multi-Risk sciEnce for resilienT commUnities undeR a changiNg climate

Codice progetto MUR: **PE00000005** – CUP LEADER PARTNER C93C22005160002

Deliverable title: Scripting for uncertainty evaluation

Deliverable ID: 2.4.8

Due date: November 30th 2024

Submission date: November 30th 2024

AUTHORS

Simone Bizzi (UniPD); Andrea Brenna (UniPD); Xue Chen (UniPD); Ebrahim Ghaderpour (Sapienza); Valeria Lo Presti (UniPA); Viviana Mangraviti (UniPD); Nicolò Parrino (UniPA); Alberto Armigliato (UniBO); Silvia Ceramicola (OGS); Melania De Falco (UniNA); Carlo Esposito (Sapienza); Giovanni Forte (UniNA); Lucia Mele (UniNA); Fabio Rollo (Sapienza); Rita Tufano (UniNA); Filippo Zaniboni (UniBO)

1. Technical references

Project Acronym	RETURN
Project Title	multi-Risk sciEnce for resilienT commUnities undeR a changiNg climate
Project Coordinator	Domenico Calcaterra UNIVERSITA DEGLI STUDI DI NAPOLI FEDERICO II domcalca@unina.it
Project Duration	December 2022 – November 2025 (36 months)

Deliverable No.	DV 2.4.8
Dissemination level*	PU
Work Package	WP4 - Trigger-based multiple geohazard scenarios
Task	T 2.4.4 - Reliability and uncertainness of statistical solutions. Uncertainty assessment methods, based on back analysis of event distribution, for ensemble and single process as well as for coupled/cascade multiple triggers.
Lead beneficiary	UniPD
Contributing beneficiary/ies	UniPD, UniRoma1, UniPA, UniNA, OGS, UniBO

* PU = Public

PP = Restricted to other programme participants (including the Commission Services)

RE = Restricted to a group specified by the consortium (including the Commission Services)

CO = Confidential, only for members of the consortium (including the Commission Services)

Document history

Version	Date	Lead contributor	Description
0.1	15/11/2024	S. Bizzi (UniPD); A. Brenna (UniPD); X. Chen (UniPD); E. Ghaderpour (Sapienza); V. Lo Presti (UniPA); V. Mangraviti (UniPD); N. Parrino (UniPA); A. Armigliato (UniBO); S. Ceramicola (OGS); M. De Falco (UniNA); C. Esposito (Sapienza); G. Forte (UniNA); L. Mele (UniNA); F. Rollo (Sapienza); R. Tufano (UniNA); F. Zaniboni (UniBO)	Final draft for Spoke review
0.2	25/11/2024	S. Martino, F. Bozzano (Sapienza); D. Calcaterra, D. Di Martire (UniNA)	Critical review and edits for approval
1.0	30/11/2024	S. Bizzi (UniPD); A. Brenna (UniPD); X. Chen (UniPD); E. Ghaderpour (Sapienza); V. Lo Presti (UniPA); V. Mangraviti (UniPD); N. Parrino (UniPA); A. Armigliato (UniBO); S. Ceramicola (OGS); M. De Falco (UniNA); C. Esposito (Sapienza); G. Forte (UniNA); L. Mele (UniNA); F. Rollo (Sapienza); R. Tufano (UniNA); F. Zaniboni (UniBO)	Final version

2. ABSTRACT

This deliverable presents the second output of Task 2.4.4, part of the WP 2.4 "*Trigger-based multiple geohazard scenarios*" focused on analysing the reliability and uncertainty of statistical methods in assessing ground instabilities under various environmental conditions.

Following guidelines established in DV 2.4.7, the working groups examine uncertainty quantification through real-world case studies, which focus on using tools and toolchains to evaluate ground instability in specific geohazard-prone environments. Each study addresses the uncertainties stemming from input data and modelling procedures. Key factors influencing the response of each environment—such as peak ground acceleration (PGA) and preparatory conditions—were defined to support consistent comparisons across contexts.

The document is structured around three primary case studies, with each chapter dedicated to a specific environmental application:

- Mountain and Hill Contexts: a toolchain was developed to evaluate shallow soil slides triggered by seismic events, considering rainfall as a preparatory factor.
- Plain Context: a tool assesses soil liquefaction potential under seismic conditions, with a case study in the Emilia-Romagna region, where factors such as groundwater depth and earthquake energy are analysed.
- Marine Context: tools evaluate the detachment and sliding of submarine landslides, with a focus on tsunamigenic potential.

These applications serve as examples towards more advanced approaches to uncertainty assessment in geosciences, providing insights into the impact of uncertainties on model outputs and practical recommendations for managing complexity in geohazard modelling. The findings and recommendations will inform Deliverable DV 2.4.9, which will further address best practices for applying and interpreting results in the context of ground instability assessments

3. Table of contents

List of Figures

4. First Chapter: Introduction

4.1 Overview of Task T 2.4.4 and deliverable DV 2.4.8

This deliverable represents the second output of the Task 2.4.4 research having as its topic "*Reliability and uncertainness of statistical solutions. Uncertainty assessment methods, based on back analysis of event distribution, for ensemble and single process as well as for coupled/cascade multiple triggers*". The task is part of the WP 2.4 "*Trigger-based multiple geohazard scenarios*". As mentioned in the Executive Working Plan (Milestone 2.1), the Task 2.4.4 "*is focused on the definition of contexts and indicators mostly affected by uncertainty (DV 2.4.7,* completed in May 2024*), the coding of procedures for the assessment of such uncertainties (DV 2.4.8), and the determination of uncertainty ranges with stochastic and/or deterministic methods (DV 2.4.9)*". In order to conduct this in-depth analysis on the topic of uncertainty "*the task will develop its products by looking at the outcomes of Tasks 2.4.1, 2.4.2, 2.4.3, and of related tasks in different WPs of Spoke 2 and of interacting Spokes. The considered environments will span from slope and river systems to submarine mass wasting, as well as alluvial plains and sea floor stability*". Deliverables DV 2.4.8 and DV 2.4.9 collectively conclude Project Milestone 2.4, titled "Proof of Concept for Seamless Integration of Projections and Uncertainty Assessment".

In accordance with what was mentioned in the previous paragraph, this deliverable represents a first systematic collection of the results obtained to date by the task groups of Spoke 2, and in particular of WP 2.4, regarding the applications of tools and toolchains for evaluating ground instabilities in different physiographic and geo-morphological contexts, with a specific focus on uncertainty quantification and sensitivity analysis.

The development of the work was structured starting from the guidelines provided within the deliverable DV 2.4.7, completed in May 2024, in which the uncertainties working group provided a general (i.e., valid for both for marine and terrestrial environments and the relative working tools) workflow aimed at providing best practices and concrete steps to deal with the main and different sources of uncertainty to which the evaluation of ground instabilities in terms of occurrence, dynamics, effects etc. is subjected. Working groups involved in the development and application of tools and toolchains in various environmental contexts (i.e., T 2.4.1: near-shore, coastal, and volcanic island, T 2.4.2: hilly and mountain areas, T 2.4.3: large plains) were asked to apply their research products to real-world case studies in order to specifically assess the effects of uncertainties in input data and modelling procedures on the results obtained.

In order to make the applications to the various physiographic and geo-morphological contexts as comparable as possible, a single factor was chosen as the main trigger for the ground instabilities considered in the various environments. Specifically, a seismic trigger was chosen, thus considering the processes potentially triggered by an earthquake whose peculiar characteristics (e.g., peak ground acceleration, PGA) were defined in each application. In each application, the various predisposing and preparatory factors for the occurrence (or possible inseverance) of the ground instabilities considered are then defined.

The document is organised through three macro applications, for each of which the authors have briefly reported on how the tools and toolchains work, the results obtained in the case studies considered, and specific comments about how the sources of uncertainty were considered and their impact on the outputs.

In more detail, the chapters are as follows:

- **Second Chapter**: Applications of tools and toolchains for evaluating ground instabilities in mountain and hill contexts, with a focus on uncertainty quantification and sensitivity analysis (Edited by C. Esposito, F. Rollo, and R. Tufano). The application considers a toolchain developed for the study of shallow soil slides in the mountain-hill environment activated by the occurrence of a seismic event. In this case study, special

attention is also paid to the preparatory factors prior to the occurrence of the earthquake, as the developed toolchain is able to evaluate the insevering effects produced by rainfall. The case study considered is the basin of the Mignone River (Italy).

- **Third Chapter**: Applications of tools and toolchains for evaluating ground instabilities in plain contexts, with a focus on uncertainty quantification and sensitivity analysis (Edited by G. Forte, M. De Falco, and L. Mele). The application considers a tool used to characterize the liquefaction processes, defined as a phenomenon that occurs when saturated soils lose strength due to seismic shaking, depends on various preparatory (i.e., depth of groundwater table) and triggering (energy of earthquake) factors. The tool is applied to test area located in the Emilia-Romagna Region.
- **Fourth Chapter**: Applications of tools and toolchains for evaluating ground instabilities in marine (near-shore and coastal environments) contexts, with a focus on uncertainty quantification and sensitivity analysis (Edited by F. Zaniboni, S. Ceramicola, and A. Armigliato). The application considers tools and parameters used to explain the processes of detachment and sliding of a submarine landslide along an open slope located near the coastal area, with a focus on the quantification of the related tsunamigenic potential. The tools are applied to the Assi landslide complex, located in the Ionian Calabrian Margin.

Considering that this type of uncertainty assessments turns out to be relatively uncommon in the field of geoscientific applications, the results obtained in these case studies represent useful examples for the development of applied research on ground instabilities and for consciously using the results obtained in the field of applications. The three macro-applications are developed following a scenario-based approach, wherein the input data and model parameters are selected on a case-by-case basis by the expert authors specializing in the specific ground instabilities under consideration. This work does not assess the quality of the scenarios, it is not the aim of this exercise to evaluate if a scenario is more likely of another, but rather addresses the epistemic uncertainty arising from them. Indeed, ground instability models can be validated on past events, but they are often used to forecast the likeness of specific instabilities to occur in the near future. In this context it is not possible to validate model simulations, it is instead possible to discuss which range of future conditions (e.g., preparatory and predisposing factors) are more likely. Deliverable DV 2.4.9 will focus on the implications of uncertainty on modelling and forecasting ground instabilities, and their practical applications. It will also address best practices for managing such complexities, including the adoption of methodologies that extend beyond reliance on simple expert judgment for scenario selection.

5. Second Chapter: Applications of tools and toolchains for evaluating ground instabilities in mountain and hill contexts, with a focus on uncertainty quantification and sensitivity analysis

Edited by: C. Esposito, F. Rollo, and R. Tufano

5.1 Introduction

This document is a contribution to the deliverable "DV 2.4.8 - Scripting for uncertainty evaluation" (PNRR - PE3 RETURN), concerning the quantification of uncertainties in the use of the tools proposed in the previous phases of the project for the development of the Proof of Concept (PoC).

For the purposes of DV 2.4.8 (and therefore with particular reference to the management of uncertainties in the input and output of calculation models) a toolchain applied to a real case study has been tested. This pilot study concerned the definition of a scenario of ground instability, starting from the knowledge of the intrinsic predisposition of the territory to landslides (susceptibility), passing through the evaluation of the inseverance of the predisposition conditions due to a preparatory factor (rainfall) of an arbitrarily selected intensity, and arriving at the evaluation of the further inseverance due to seismic shaking, also of an intensity defined in a "deterministic" manner. It should be noted in this introduction that the choice of "arbitrary" intensity levels of preparatory (rain) and triggering (earthquake) processes derives from the shared decision not to treat these types of input in probabilistic terms, since it is not the subject of VS2, which is instead called upon to define event scenarios for intensity levels of preparatory and triggering processes defined elsewhere (e.g., by other Spokes).

5.2 Environmental context

5.2.1 General framework of the study area

The case study relates to the catchment area of the Mignone river in northern Latium (Italy). This area is part of a continental context characterized by hilly altitudes, but which locally presents steep morphologies and high relief energies due to the volcanic lithotypes present in the area and the high resistance to erosion by the more lithoid facies. Based on institutional databases (https://idrogeo.isprambiente.it/app/), the basin is also characterized by large areas defined as moderate to very high landslide susceptibility, to which attention areas must also be added. It is therefore a context characterized overall by a high susceptibility to landslides (Figure 5.1).

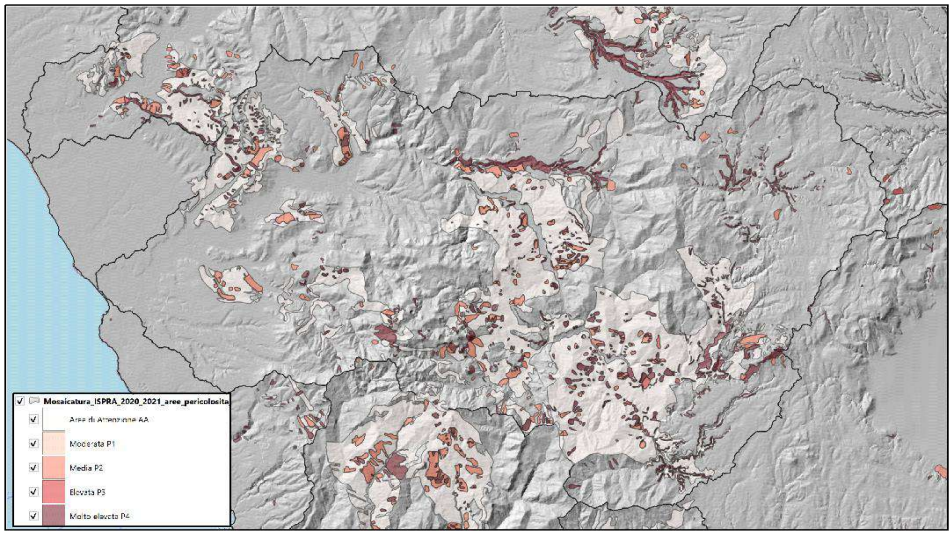

Figure 5-1 Excerpt from the official landslide hazard map (Piano di Assetto Idrogeologico) as published on the website https://idrogeo.isprambiente.it/app/

With regard to the type of landslides present in the area, from the IFFI database, exemplified in the cartographic excerpt below (Figure 5.2), it is possible to deduce the presence of large areas affected by shallow landslide phenomena that mobilize the eluvial-colluvial layers. Since these processes are particularly sensitive to the action of rainfall (both as a preparatory and triggering factor) and earthquakes, it was decided to test one of the toolchains rationalized for this type of ground instability.

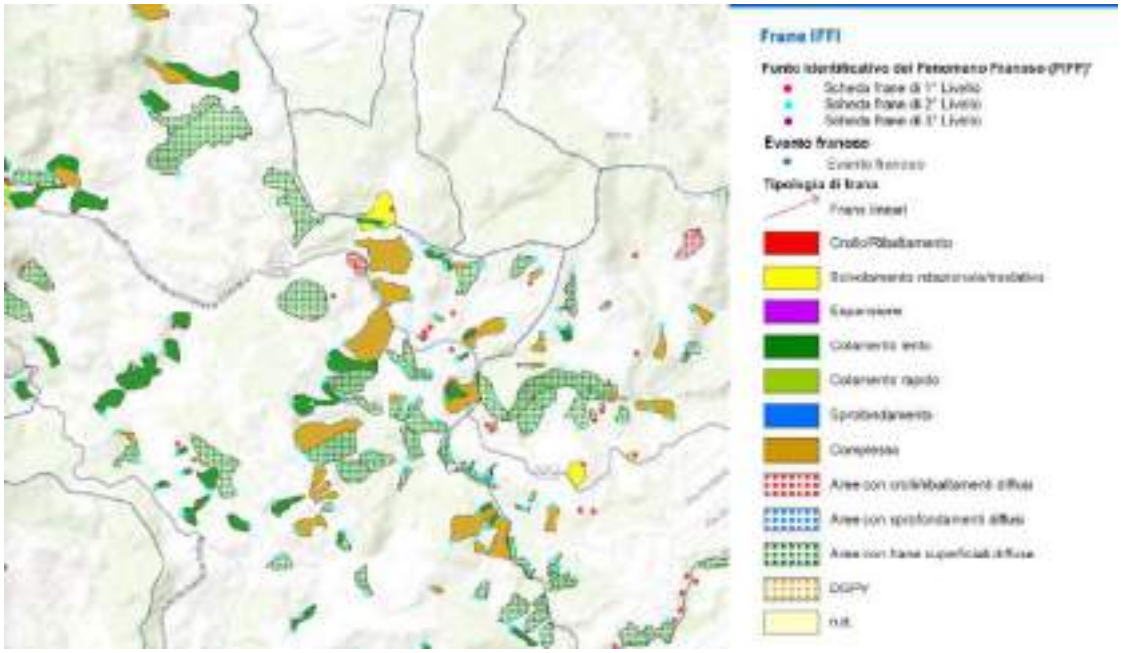

Figure 5-2 Types of landslides present in the area extracted from the IFFI database.

5.2.2 Case study and analyzed ground instability

As mentioned in the introduction, the functioning of a complete toolchain was tested to define a scenario of seismically induced shallow landslides prepared by an antecedent rainfall event.

In summary, therefore, these are the salient features of the case study:

- Environment: hill-mountain
- Instability category: landslide
- Study scale: river basin
- Test site: Mignone river basin
- Kinematic: rapid
- Instability type: shallow soil slides
- Trigger category: earthquake
- Preparatory process: rainfall
- Predisposing factors: lithology, DTM-derived morphometry and soil cover

5.2.3 Notes on the functioning of the tools implemented

The toolchain adopted consists of the following operational tools:

i) Tool for susceptibility assessment

This is a tool developed within the Spoke VS2 WP2. Starting from ancillary datasets relating to predisposing factors and inventory information on ground instabilities, it provides a susceptibility assessment by means of different statistical methods: from bivariate methods to machine learning (ML). The choice also depends on the numerosity of the input data, which is particularly relevant for the implementation of ML techniques. Depending on the technique adopted for susceptibility assessment, the output metrics can refer to a spatial probability of positive outcome (landslide) in the future (in the case of multivariate statistics or ML) or to the sum of contributions of each single predisposing factor to the overall susceptibility of that grid cell.

ii) **Tool for assessing the hydraulic condition of slopes as a result of rainfall and related infiltration/seepage**

Use was made of an open-source, GIS-based tool (https://grass.osgeo.org/grass84/manuals/r.topmodel.html), to assess the water table depth and, thus, of the pore water pressure in the shallow layers of the slopes. TOPMODEL (Beven et al., 1995) is a physically based, distributed watershed model that simulates hydrologic fluxes of water (infiltration-excess overland flow, saturation overland flow, infiltration, exfiltration, subsurface flow, evapotranspiration, and channel routing) through a watershed. The model simulates explicit groundwater/surface water interactions by predicting the movement of the water table. Even if simplified, beyond an input rainfall such a model requires a relevant number of quantitative information, especially in terms of geotechnical (physical) and hydrogeological/hydraulic parameters.

iii) **Tool for the physically-based analysis of slope stability conditions due to preparatory rainfall (antecedent scenario)**

Clusters of pixels over a fixed susceptibility threshold are subject to the slope stability assessment based on limit equilibrium method and according to the infinite slope model (implemented in a simple GIS-based raster calculation); the presence of water (output of previous step) has been accounted for only in terms of hydrostatic pore pressure, thus neglecting seepage forces as well as suction effects. The results can be used to define the location of: i) unstable slopes for hydrostatic forcing (areas with FoS $\leq$ 1), ii) stable areas but close (1 < Fos $\leq$ custom threshold) to limit equilibrium. The latter are subject to the analysis of the subsequent tool(set). This simplified model also requires a relevant number of quantitative information, such as: geotechnical (both physical and mechanical) parameters and information about soil depth and terrain slope.

Tool for the evaluation of co-seismic displacements (trigger-based scenario). Such a tool is in turn composed by a sequence of operations, namely:

- calculation of Ky (pseudo-static critical horizontal acceleration)
- Semi-empiric evaluation of expected co-seismic displacements

In detail, the calculation of the yield seismic coefficient at a) is performed according to the scheme of infinite slope, able to account for shallow and translational sliding mechanism at a very limited computational cost. This allows to use the values of Ky for the calculation of co-seismic displacements through a recent semi-empirical relationship (Rollo and Rampello, 2023) as a function of the magnitude of the strong motion (i.e., PGA and PGV) as per the point b).

5.2.4 Description and outputs of the tested tools

Tool for susceptibility assessment

The analysis provides a raster map of Susceptibility values: a numerical value is assigned to each grid cell quantifying its spatial proneness to landslide. For this case study, due to the limited number of information (i.e., number of inventoried landslides) not suitable for ML algorithms, the Frequency ratio technique has been implemented. Thus, a binary classification of the Landslide Susceptibility Index (sum of Frequency Ratio values of each class of every variable on a cell-by-cell basis) was performed according to the Detection Rate Curve, obtained by sampling the LSI raster at the points of known landslide location (Figure

5.3 and Figure 5.4). The threshold has been put to a value corresponding to the 50% of correct predictions. The predisposing variables (retrieved / elaborated from institutional databases) considered in this test are:

- Lithology
- Soil cover
- Geomorphic domain class
- Slope
- Distance to streams
- Elevation
- Stream power index

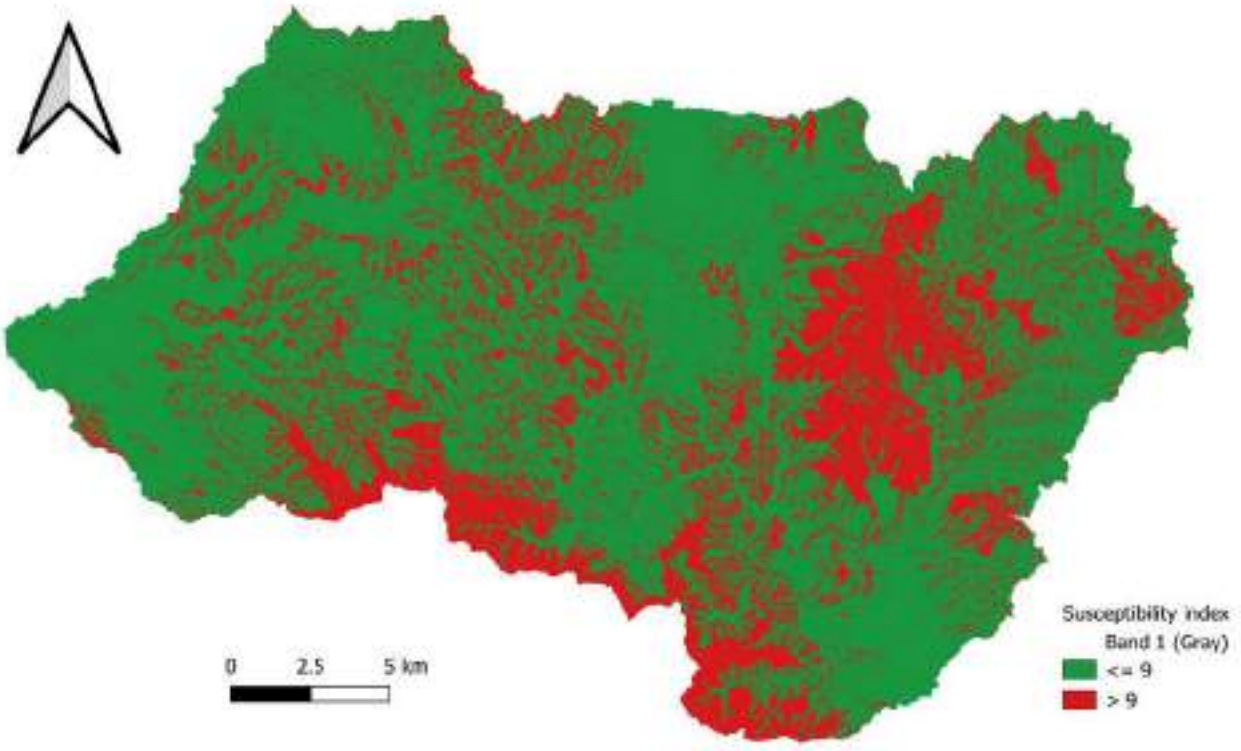

Figure 5-3. Binary map of susceptibility to shallow landslides in the Mignone river basin. Red areas are featured by cluster of pixels beyond a selected susceptibility threshold chosen on the basis of the Detection Rate Curve.

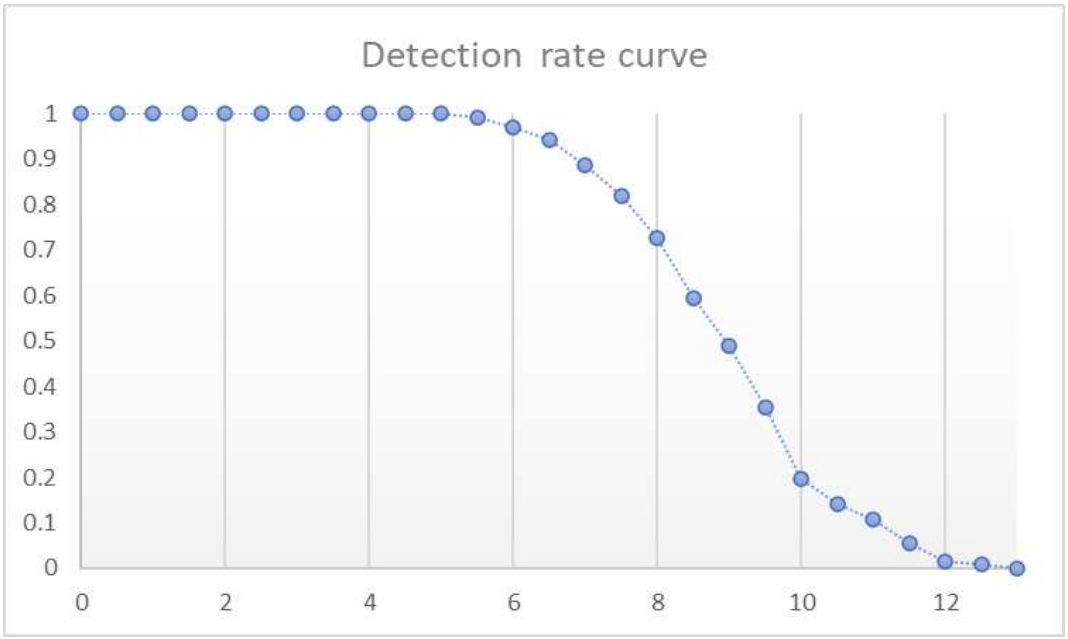

Figure 5-4. Detection rate curve (LSI values on the x-axis and cumulated proportion of correct predictions on the y-axis).

Tool for assessing the hydraulic condition of slopes as a result of rainfall and related infiltration/seepage

The relevant output of TOPMODEL for this toolchain is a raster map where each pixel assumes a value coinciding with the assessed depth below ground level of the water table arising from infiltration in the shallow soil (Figure 5.5).

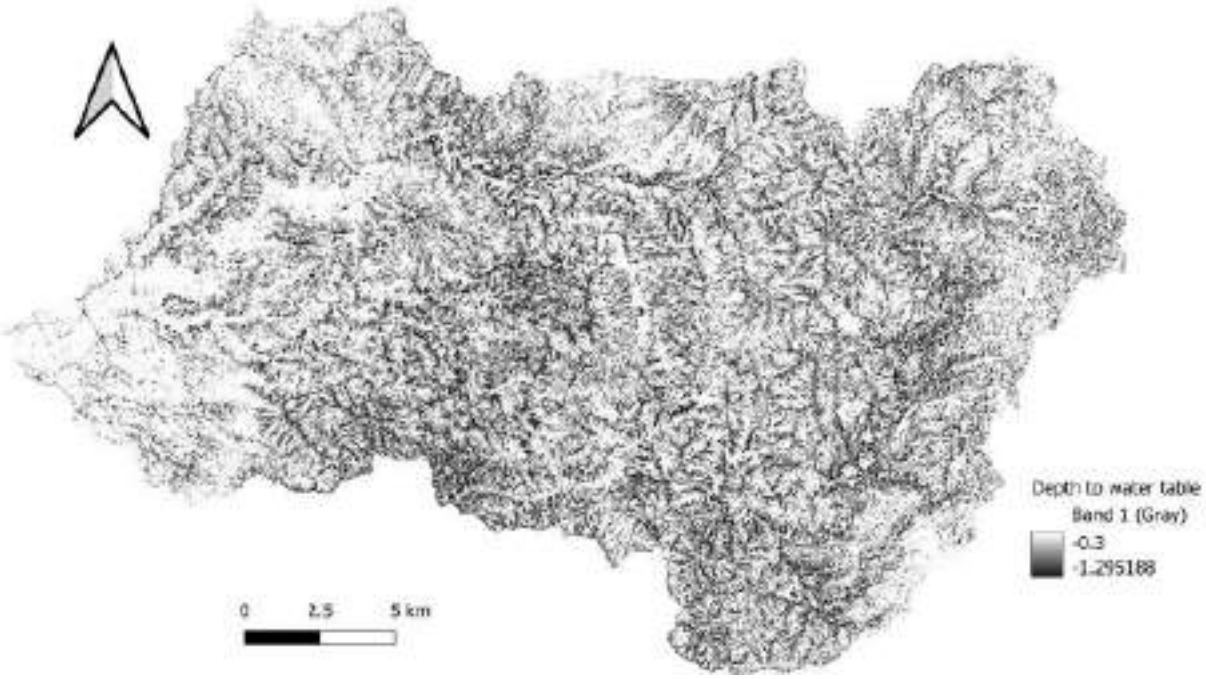

Figure 5-5. Map of estimated water table depth (for a specific rainfall input, equal to 30 mm of antecedent rainfall for this test)

Tool for the physically-based analysis of slope stability conditions due to preparatory rainfall (antecedent scenario)

The GIS-based procedure implemented for quantifying the factor of safety results in a raster map where each pixel assumes the FoS value resulting from the limit equilibrium analysis for an infinite slope (Figure 5.6). In this test the presence of water has been considered only in terms of hydrostatic pore pressure, thus neglecting seepage forces as well as suction effects. The output map has been reclassified to point out unstable areas under static conditions (FoS < 1) and metastable areas (1 < FoS ≤ 1.5). Clusters of pixels with 1 < FoS ≤ 1.5 define the analysis units for the subsequent definition of the trigger-based scenario.

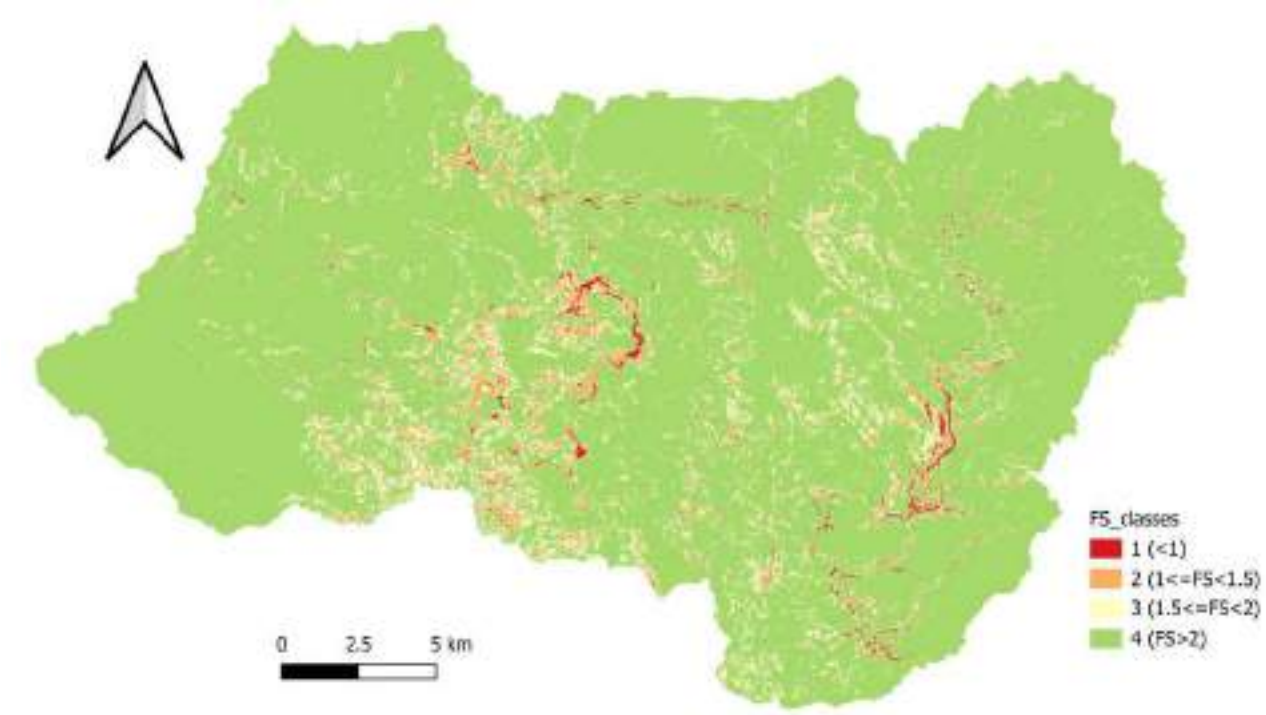

Figure 5-6. Map of estimated Factor of Safety classes (for a specific combination of input parameters values)

Tool for the evaluation of co-seismic displacements (trigger-based scenario)

Each cluster of pixels with 1 < FoS ≤ 1.5 (output of previous tool) feature a polygon that can be considered as potential first-activation landslide under dynamic forcing. To assign a unique set of input values to each polygon for the co-seismic analysis, the GIS-based zonal statistic tool has been applied to retrieve statistically significant parameters (mean, median and standard deviation for DTM-dependent parameters and majority, minimum and maximum for parameters derived from categorical information). The result has been exported in csv format for the subsequent analysis exploiting calculated fields:

- The ky values for each row (corresponding to a polygon)
- The semi-empiric evaluation of expected co-seismic displacements for rows (each corresponding to a polygon) with Ky < PGA has been performed according to the two semi-empirical relations. The PGA value was chosen to be 0.15g. The value of PGV to be introduced in the vector relationship was evaluated on the basis of the regression shown in the Figure 5.7 below, obtained on the basis of the characteristics of the Italian seismic database. This resulted in a reasonable pair of PGA, PGV.

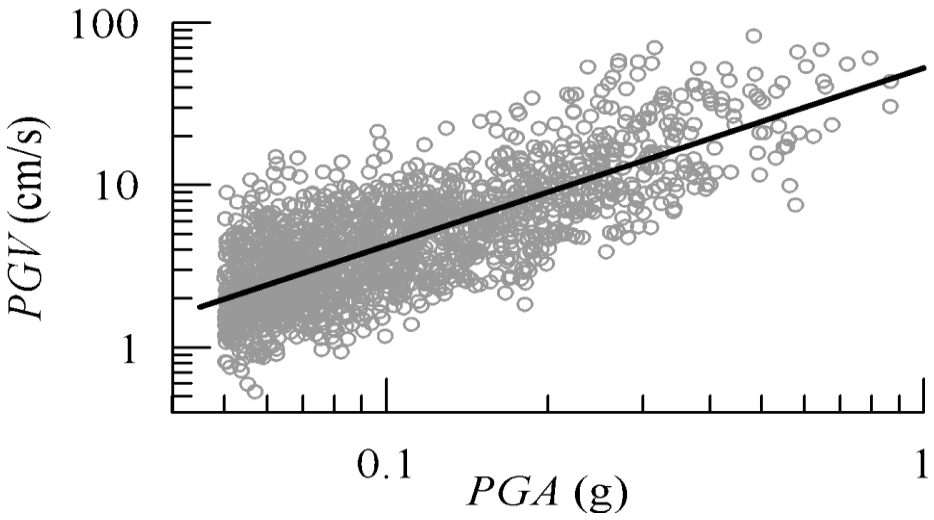

Figure 5-7. Regression between PGA and PGV values obtained on the basis of the characteristics of the Italian seismic database.

5.3 Sources of uncertainty, proposed and implemented strategies

Susceptibility assessment

"Native" outputs of the susceptibility assessment are featured by ROC curves (and related metrics) or Detection Rate Curves (depending on the technique adopted) that allow users to somehow quantify the uncertainty (specificity and sensitivity of the predictive model) related to susceptibility classes once the latter are estimated from the continuous results.

Assessment of hydraulic conditions of slopes due to rainfall

Beyond the intrinsic potential uncertainty related to the hazard of the input rainfall, uncertainties can arise from the following issues:

- rainfall is homogenously distributed over the area. It is quite difficult to quantify this potential error, that can be partially overcome if the area is partitioned into sub-areas reflecting, for instance, the Thiessen polygons of rain gauges.
- The amount of seepage and, then, the water table location is strongly affected by hydraulic parameters assigned to soil layers.

Possible strategies to overcome the issues are:

- Calibration, if ground truth data are available
- Sensitivity analysis, if a (bibliographic) range of values is available

Antecedent scenario

Many sources of uncertainty affect this kind of physically based analysis and are related to the variability of geotechnical (unit volume weight, soil cohesion, [root cohesion, if taken into account], friction angle) and geometric (mobilizable soil thickness) parameters.

Possible strategies to overcome the issues are:

- Calibration, if ground truth data are available
- Probabilistic stability analysis to account for the known or modelled parameter variability
- Sensitivity analysis, if a (bibliographic) range of values is available

For this test we performed a sensitivity analysis considering a "reasonable" range of each parameter value. Comparing the results of each combination of input parameters can result in a map providing information

on the variability of outcomes (expressed of ±% variation with respect to the reference result, e.g., based on average parameters).

The sensitivity was assessed by analysing the changes with respect to a standard value resulting from the variation of the generic i-th independent variable (Xi) with respect to its basic value (XiR), while keeping all the other parameters (Xj) constant for $j \neq i$. Therefore, to provide perspectives on the key drivers generating the FS map for the Bonis catchment, the sensitivity was assessed by changing the following parameters:

- Cohesion
- Friction angle
- Soil unit weight
- Root cohesion
- Water Unit Weight

By applying the "one-factor-at-a-time" method OAT, each parameter was changed by ±5% and ±10% from the standard value. Moreover, the changing of parameter values potentially reveals a linear (or non-linear) relationship among the parameter changes and model output, as well as the sensitivity of each parameter at different times during the simulation. This methodology shows the relative change of FS (ΔCF_{CG}) for the variation of each parameter with respect to the reference value (CF_{CGR}). CF_{CGR} value was plotted against the relative variation of each independent parameter Xi accounted for (ΔXi) with respect to the corresponding reference value (XiR) to assess its slope mi as defined by:

$$Smi=(\Delta CF_{CG}/\underline{CF_{CGR}})(\Delta Xi/Xi_R)$$

where, *mi* is the partial derivate of FS compared to its reference value (FSR) with respect to the relative variation of the i-th parameter (Xi) compared to its reference value (XiR). As such, the intrinsic linearity of the above Equation was immediately checked (Figure 5.8). Thus, for higher values of mi, the sensitivity of FS towards the relative variation of Xi is also higher.

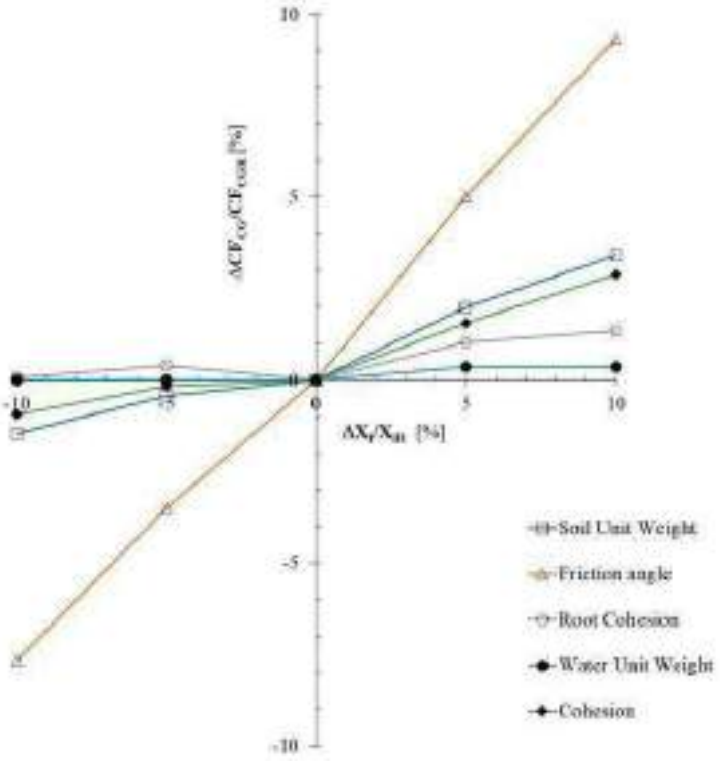

Figure 5-8. Plot of the sensitivity analysis results. See text for a detailed explanation.

Trigger-based scenario

Possible sources of uncertainty are: geotechnical (unit volume weight, soil cohesion, [root cohesion, if taken into account], friction angle) and geometric (mobilizable soil thickness) parameters adopted for computing Ky. Furthermore, each polygon representing a "critical" slope section (i.e., in a specific range of FoS greater than 1) encompasses clusters of cells with (potentially) variable parameters (and related uncertainty). Possible strategies to account for uncertainty are as follows:

- Performing as many analyses as those considered for the assessment of FoS. Comparing the results of each combination of input parameters can provide information on the variability of outcomes (expressed of ±% variation with respect to the reference result, e.g., based on average parameters). Furthermore, each polygon can be featured by average geotechnical and geometrical values as well as by other statistically controlled values (e.g., maximum, minimum, a specific percentile, etc.). The uncertainties of the former input parameters can be condensed in a variation of the yield seismic coefficient Ky.

- For a given value of PGA (and possibly PGV), one (or two) semi-empirical relationships can provide the values of the co-seismic displacements for a wide range of Ky to quantify the uncertainty of the slope geometry and the physical and mechanical properties of soils on the displacements.

- Another level of uncertainty can be assessed considering different percentiles of the displacement semi-empirical relationship for a fixed value of PGA (or a_{max}). The coefficients of the semi-empirical relationship, developed with reference to the Italian seismicity, can be set to reproduce the median distribution of the permanent displacements shown in the Figure 5.9 (the latter computed through the Newmark's method for a broad range of Ky and for all the horizontal acceleration time-histories of the Italian strong motion database) or to account for upper-bound solutions related to different percentiles according to a normal probability distribution. As per example, in the Figure 5.9 are shown the semi-empirical relationships for 50th (median) and 94th percentile, but the results for other values of percentiles greater than 50th can be provided.

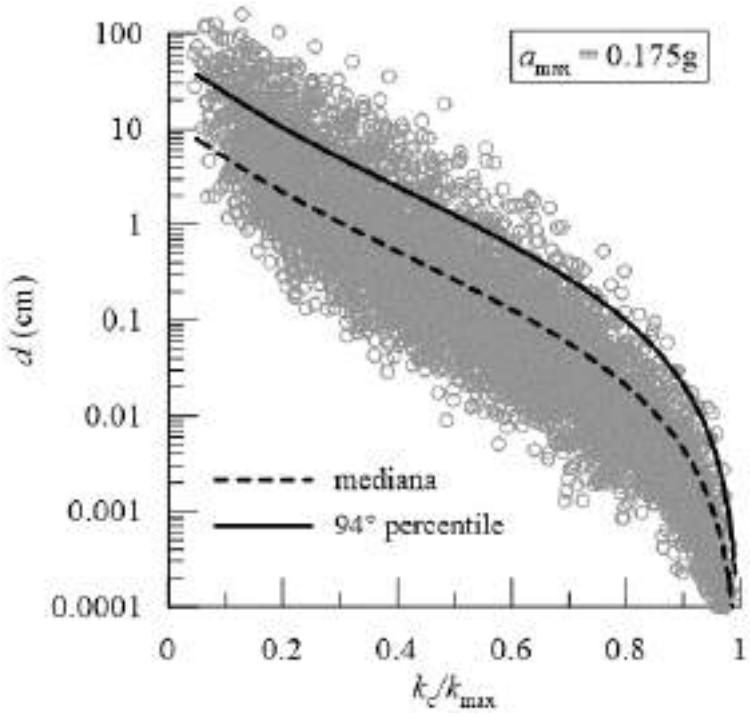

Figure 5-9. Plot showing the semi-empirical relationships K_y/K_{max} – co-seismic displacement for 50th (median) and 94th percentile.

- For a specific site with a given level of seismic hazard, for any values of Ky a displacement hazard curve can be obtained, showing the annual rate of exceedance of the occurrence of a co-seismic displacement (or, similarly, its inverse, the return period) within a wide range of displacement values, as shown in the Figure 5.10. This also allows to associate a certain threshold displacement and a value of Ky to a given probability of occurrence in a given interval of time, say the return period, to which corresponds a specific limit state according to the current Italian building codes.

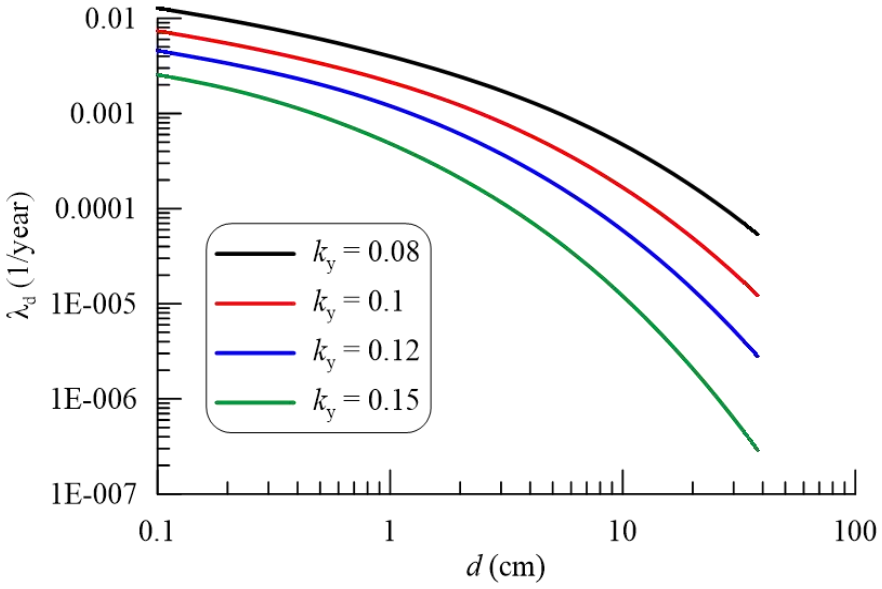

Figure 5-10. Displacement hazard curves for a set of different Ky values

In this testcase only the Ky coefficients were evaluated for the combination of minimum, average and maximum c‘ (soil + root) and φ’, as the sensitivity analysis of trigger-based scenario tool highlighted their relevance. As a result, a set of 6 co-seismic displacements was computed for each potential landslide polygon: 3 combinations of strength parameters x 2 semi-empirical relations (Table 5.1).

Table 1. Estimated co-seismic displacements for a random subset of potential co-seismic landslides. The six value fields refer to the results obtained by the two semi-empirical relationships ('d,scalar' and 'd,vector) for three different combinations of morphological and geotechnical parameters (namely minimum, mean/mode, maximum values)

	MIN		MEDI		MAX	
ID	d,scalar (cm)	d,vector (cm)	d,scalar (cm)	d,vector (cm)	d,scalar (cm)	d,vector (cm)
4996	0	0	0	0	0	0
5015	inf	inf	0.429594	0.433372	0	0
5061	0.075173	0.078616	0.075173	0.078616	0.075173	0.078616
5153	0.607549	0.605221	0.607549	0.605221	0.607549	0.605221
5156	inf	inf	0.677795	0.672327	0.078197	0.081759
5247	0	0	0	0	0	0
5252	0.132549	0.137757	0.132549	0.137757	0.132549	0.137757
5261	inf	inf	0.012418	0.012809	0	0
5285	0	0	0	0	0	0
5317	0.100539	0.104879	0.100539	0.104879	0.100539	0.104879
5329	5.71E-07	3.84E-07	5.71E-07	3.84E-07	5.71E-07	3.84E-07
5338	0.211141	0.217433	0.211141	0.217433	0.211141	0.217433
5339	0.058731	0.061486	0.058731	0.061486	0.058731	0.061486
5344	0	0	0	0	0	0
5381	0.00155	0.001502	0.00155	0.001502	0	0
5471	0	0	0	0	0	0
5472	0	0	0	0	0	0
5515	0	0	0	0	0	0
5607	0	0	0	0	0	0
5610	inf	inf	0.102295	0.10669	0	0
5650	2.525838	2.371849	0.001301	0.001252	0.001301	0.001252

5.3 Discussion and Conclusions

When applying a toolchain, the "uncertainty issue" becomes much more relevant to the extent uncertainties of a single tool propagates to those successive, that receive uncertainties and produce even further uncertainties.

In the testcase here presented we used a sequence of tools that natively do not implement proper probabilistic outputs nor deal with probabilistic inputs. In such case sensitivity analyses are the only feasible actions to try to constrain uncertainties. Notwithstanding, relevant issues still remain, especially when a model runs with a significant number of input data, which imply a potential factorial combination of parameters and related values to be considered. Furthermore, even if a sensitivity analysis suggests the more relevant category/ies of input data, in case of lack of calibration / validation scenarios it is not trivial to assess which parameter value (or combination of parameters) is more representative of the actual conditions.

Thus, at least an expert judgment to "model" the distribution of parameter variability is needed to associate a PDF in order to link a probability of occurrence for each value tested in the sensitivity analysis: this is a possible way to manage "multinomial" results, associating a probability / likelihood of each resulting scenario, in turn related to the PDFs of the input parameters.

6. Third Chapter: Applications of tools and toolchains for evaluating ground instabilities in plain contexts, with a focus on uncertainty quantification and sensitivity analysis

Edited by G. Forte, M. De Falco, and L. Mele

6.1 Introduction

This document is a contribution to the deliverable "DV 2.4.8 - Scripting for uncertainty evaluation" (PNRR - PE3 RETURN), which is focused on the quantification of uncertainties related to the tools and methodologies developed in earlier phases of the project for the Proof of Concept (PoC). Specifically, this work concentrates on the evaluation of uncertainties associated with the assessment of liquefaction potential in plain areas, a critical aspect of seismic hazard mitigation.

The goal of this study is to outline the key conceptual steps undertaken to quantify the uncertainties linked to the tools and parameters used to explain the liquefaction process. Liquefaction, a phenomenon that occurs when saturated soils lose strength due to seismic shaking, depends on various preparatory and triggering factors, which exhibit natural variability. These uncertainties can affect the accuracy of predicting liquefaction risk and must be thoroughly considered in any hazard assessment.

To estimate the uncertainties associated with liquefaction in plain areas, the focus was placed on two critical factors: the preparatory factor (groundwater table) and the triggering factor (Peak Ground Acceleration, or PGA). Both factors exhibit inherent variability, which plays a key role in determining liquefaction susceptibility.

- **Groundwater Table as a Preparatory Factor**

  The groundwater table is a fundamental element in liquefaction analysis because the soil must be saturated for liquefaction to occur. The depth of the water table can vary significantly, even within small geographical areas, depending on seasonal changes, topography, and local hydrogeological conditions. To account for this variability, the groundwater table was modelled using monitoring head data, which provided information about its fluctuations over time. The uncertainty related to this factor arises from both temporal variations and spatial differences across the area being studied. In this assessment, groundwater levels ranged from the surface (field level) to varying depths, contributing to different degrees of liquefaction susceptibility depending on the local water table conditions.

- **Peak Ground Acceleration (PGA) as a Triggering Factor**

  The PGA is a measure of the maximum ground acceleration that occurs during an earthquake and is commonly used as a proxy for seismic intensity. In this study, the variability of the PGA was evaluated based on the seismic hazard zones defined for different macro-seismic areas in Italy. The uncertainty related to PGA stems from both the spatial distribution of seismic risk across different regions and the variability in earthquake magnitude, duration, and depth. Since liquefaction is triggered by strong seismic shaking, the degree of shaking represented by the PGA is crucial for determining the likelihood of liquefaction at any given location. However, due to the unpredictable nature of earthquakes, there is always uncertainty regarding the exact magnitude and distribution of seismic forces in future events.

By combining these preparatory and triggering factors, the study developed four distinct scenarios for assessing liquefaction potential. These scenarios represent different combinations of groundwater table depths and PGA values, reflecting the range of conditions that could influence liquefaction susceptibility. For example, a shallow water table combined with a high PGA represents a high-risk scenario for liquefaction, whereas a deep water table with a lower PGA would indicate a lower risk. The scenarios allow for a comprehensive analysis of how different conditions might lead to liquefaction and the uncertainties associated with predicting such outcomes. The uncertainty in these scenarios arises from two key sources:

1. **Parameter Uncertainty:** Both the groundwater table and the PGA exhibit natural variability and are subject to measurement and estimation errors. Groundwater table data, for instance, may be incomplete or imprecise due to limitations in the spatial and temporal coverage of monitoring stations. Similarly,

PGA estimates depend on probabilistic seismic hazard assessments that carry their own uncertainties related to seismic modelling and historical earthquake data.

2. **Spatial Data Distribution:** The availability of spatial data for the region also affects the uncertainty in the analysis. Liquefaction risk is not uniform across an area, and the accuracy of the assessment depends on the density and quality of available data. In areas where groundwater monitoring data or seismic records are sparse, the uncertainty in the liquefaction predictions increases, as the model must interpolate or extrapolate values based on limited information.

This methodology was applied to an area in the Emilia-Romagna Region, which has both a rich dataset of geological and hydrogeological information and a history of liquefaction events, particularly following the 2012 Emilia earthquake. The 2012 earthquake caused widespread liquefaction in the region, making it an ideal case study for evaluating the effectiveness of the liquefaction assessment tools and the associated uncertainties.

6.2 Environmental context

6.2.1 Liquefaction triggering assessment

Earthquake induced liquefaction can be simply defined as the temporary transition of a granular soil from the solid to a fluid state as a consequence of the increased pore-water pressures. The detrimental effects on structures and infrastructures put soil liquefaction among the most serious consequences of earthquakes and in the last years, there has been an increasing demand for developing liquefaction hazard maps to reduce risk for the built environment.

Liquefaction typically occurs on loose saturated sandy deposits, being their contractive tendency upon cyclic shearing inhibited by water with the onset of positive excess pore pressures (Δu).

If the net excess pore pressures build up is positive, the normal effective stresses will reduce during the seismic action, eventually increasing back during the post-seismic consolidation phase. Since the soil shear strength $\tau(\sigma')$ and stiffness $G(\sigma')$ directly depend on the effective stresses, they will progressively reduce during the seismic action on liquefiable soils, becoming nihil when the effective stresses tend to zero (full liquefaction, theoretically at ru=1). At the end of cyclic action, consolidation will take place due to the excess pore pressure drainage.

The assessment of liquefaction triggering and, more generally the response of a soil deposit in terms of pore pressure increments, can be carried out with approaches of increasing complexity, as briefly reported in Table 6.1.

Table 6.1. Analyses for liquefaction triggering assessment modified after (Silvestri and D'Onofrio, 2014).

Level of analysis	Type of analysis	Constitutive model	Calculation approach	Output
Level 1	Screening criteria (qualitative)	-	Evaluation of some parameters (grain size distribution, ground water table and expected maximum acceleration)	Liquefaction yes, no
Level 2	Semi-empirical methods	Elementary	Simplified stress-based	Actions (demand) vs. Resistance (capacity)
Level 2	Simplified dynamic analyses	Simplified (mostly visco-elastic, uncoupled)	Dynamic (with simplified geometry)	Total stresses, shear strains, pore pressure increments*
Level 4	Advanced dynamic analyses	Advanced (elasto-plastic with hardening, coupled)	Dynamic (with complex 3D geometry)	Total and effective stresses, shear strains, pore pressure increments, residual displacements
*Calculated through analytical correlations.				

Level 1 is based on the Italian Technical Standards for Constructions (NTC, 2018).

According to the NTC (2018) (Section 7.11.3.4.2), the likelihood of liquefaction occurring in saturated sandy soils is low or zero if at least one of the following conditions occurs:

- maximum expected accelerations at ground level in the absence of artefacts (free field conditions) less than 0.1g;
- average seasonal depth of the water table greater than 15 m from ground level, for sub-horizontal ground level with superficial foundations;
- deposits consisting of clean sands with normalised penetrometer resistance $(N_1)_{60} > 30$ or $q_{c1N} > 180$;
- particle size distribution outside the zones shown in Figure 6.1a in the case of soils with uniformity coefficient $U_c < 3.5$ and in Figure 6.1b in the case of soils with uniformity coefficient $U_c > 3.5$.

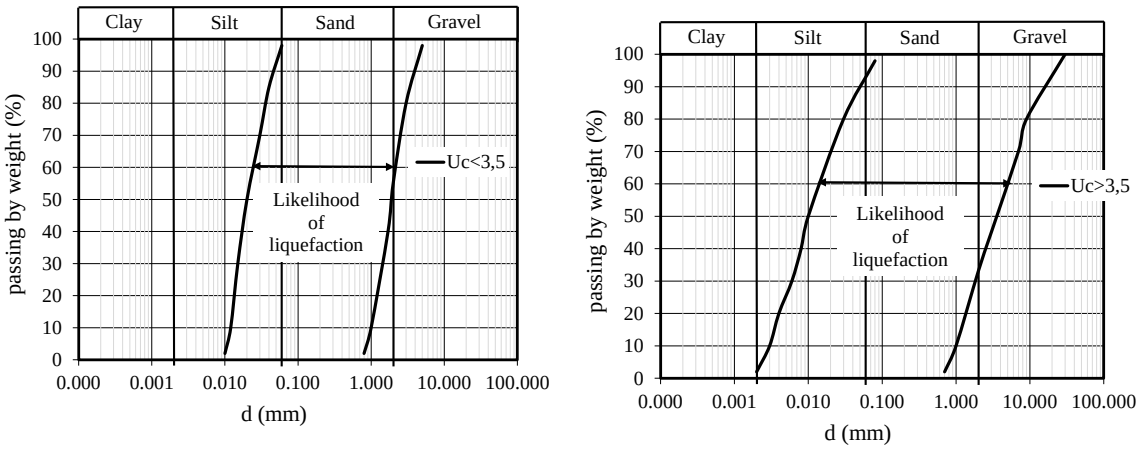

$U_c < 3.5$ (a) $U_c > 3.5$ (b)

Figure 6-1. Particle size ranges of soils susceptible to liquefaction (adapted from NTC (2018) with uniform coefficient Uc< 3.5 (a) and Uc> 3.5 (b).

If the first condition is not verified and, therefore, the maximum acceleration expected at ground level is higher than 0.1 g, the geotechnical investigations must be aimed at determining the parameters necessary to verify the other three conditions.

When none of the four abovementioned conditions is satisfied, NTC (2008) say that the site is potentially susceptible to liquefy (i.e., vulnerable, due to the presence of predisposing elements) and therefore potentially at risk (due to the non-negligible seismic hazard). It is therefore necessary to assess the liquefaction safety factor at the depths where potentially liquefiable soils are present.

Quite often in engineering practice, liquefaction triggering assessment is carried out using the semi-empirical stress-based analysis (level 2). With this approach, a factor of safety FS(z) is defined for free-field conditions (i.e. without buildings and structures) as the ratio between the normalized shear stress required to induce liquefaction (CRR=soil capacity) and the normalized equivalent stress induced by the design earthquake (CSR=demand) (Boulanger and Idriss, 2014; Seed and Idriss, 1971):

$$FS(z) = \frac{CRR(z)}{CSR(z)} = \frac{CRR_{M=7,5,\sigma'v=1}}{CSR} \cdot MSF \cdot K_\sigma \cdot K_\alpha \qquad Eq.\ 1$$

where soil capacity $CRR_{M=7.5,\sigma'v=1}$ is calculated with reference to a seismic event of magnitude M=7.5 and a vertical effective stress state of one atmosphere (101 kPa). The parameter MSF (Magnitude Scaling Factor) is a factor accounting for the effect of earthquake magnitude, and the two corrective coefficients K_σ and K_α respectively take into account the effects of vertical stress and of a possible pre-existing static shear stress on horizontal planes (e.g., sloping ground or state of stress under existing structures). Literature data (e.g. Tomasello and Porcino (2022); Vaid et al. (2001) indicate that, in loose or medium dense sands (D_r < 50%), pre-existing shear stresses reduce soil capacity. In this density range, from a practical point of view, this detrimental effect can be considered assuming K_α = 0.8.

The liquefaction resistance in free field conditions can be calculated from the results of in q_{c1Ncs} or $(N_1)_{60cs}$, which are respectively the corrected CPT tip resistance and the corrected SPT blow count counting for fine content effects (Boulanger and Idriss, 2014).

However, uncertainties in processing field tests cannot be neglected. Indeed, several formulations have been proposed in literature to calculate q_{c1Ncs} or $(N_1)_{60cs}$, it means that a unique way to calculate them does not exist (Boulanger and Idriss, 2014; Idriss and Boulanger, 2006; Idriss and Boulanger, 2008; Liao and Whitman, 1986; Robertson, 1991; Robertson and Campanella, 1985)

Similar considerations may be done for soil capacity. Several expressions have been proposed to calculate the liquefaction resistance, even though one of the most used is that of Boulanger and Idriss (2014). In this case the soil capacity referred to a magnitude M_w=7.5 and to a vertical effective stress σ'_v=103 kPa ($CRR_{M=7.5,\sigma'v=1}$) is given by:

$$CRR_{M=7.5,\sigma'v=1} = exp\left(\frac{q_{c1Ncs}}{113} + \left(\frac{q_{c1Ncs}}{1000}\right)^2 - \left(\frac{q_{c1Ncs}}{140}\right)^3 + \left(\frac{q_{c1Ncs}}{137}\right)^4 - 2.8\right) \qquad Eq.\ 2$$

$$CRR_{M=7.5,\sigma'v=1} = exp\left(\frac{N_{1,60cs}}{14.1} + \left(\frac{N_{1,60cs}}{126}\right)^2 - \left(\frac{N_{1,60cs}}{23.6}\right)^3 + \left(\frac{N_{1,60cs}}{25.4}\right)^4 - 2.8\right) \qquad Eq.\ 3$$

where q_{c1Ncs} and $(N_1)_{60cs}$ are respectively the normalized values of the tip resistance CPT and the number of blows (N_{SPT}) corrected for the fines content (FC, defined as the percentage by weight passing at the 0.075 mm sieve).

However, it should be noted that these (and other) correlations have been found to separate data where liquefaction occurs and where not. Figure 6.2 shows as field data are dispersed and then, it is easy to understand that the correlation can be affected by uncertainties.

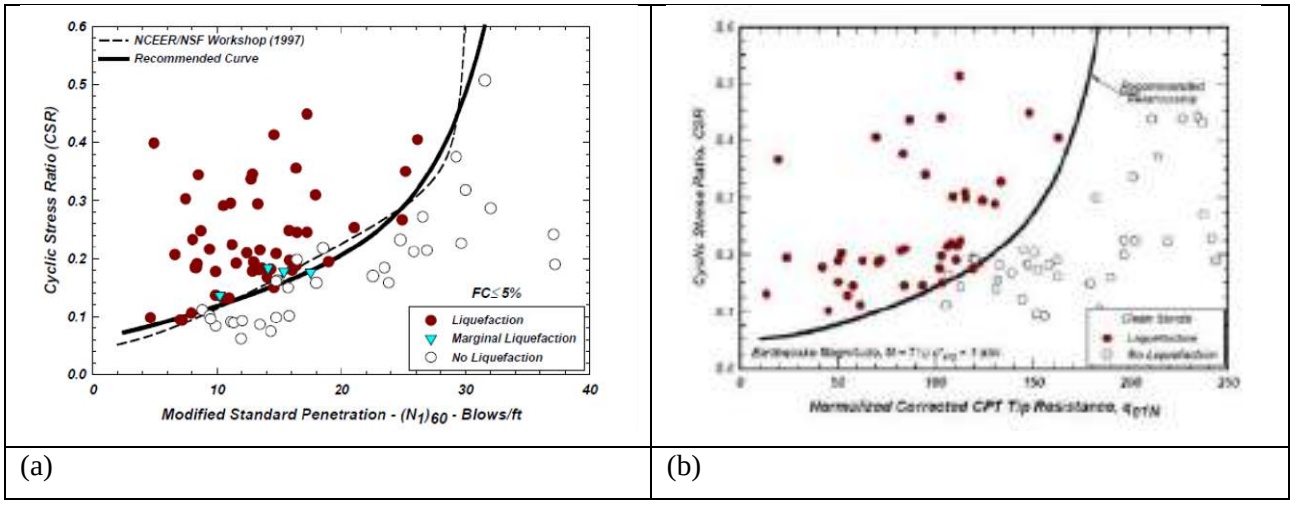

Figure 6-2. Liquefaction resistance charts for SPT (a) and CPT (b) tests (Idriss & Boulanger, 2004)

It has to be emphasized that *Eq. 2* and *Eq. 3* have no mechanical origin and are just analytical correlations empirically set up to separate historical data of liquefied from non-liquefied cases in a capacity vs. demand plane. Generally, they correspond to a conservative lower bound of the observed values of CRR, and thus lead to a conservative estimate of FS(z).

With the semi-empirical approach, the stress state induced by the seismic action is estimated through the knowledge of the maximum horizontal acceleration expected at ground level (PGA, a_{max}) according to a well-established empirical procedure, or as a(z) at the generic depth of interest, if the results of local seismic response analyses are used. Typically, with this approach the cyclic stress ratio CSR is calculated as (Seed and Idriss, 1971):

$$CSR(z) = 0.65 \frac{a_{max}}{g} \frac{\sigma_v}{\sigma'_v} r_d \qquad Eq.\ 4$$

where σ_v and σ'_v are the total and effective lithostatic stress at the generic depth (z), a_{max} is the peak value of the expected horizontal acceleration at the surface, g is the earth's gravitational acceleration and r_d is a reductive factor of the acceleration to take into account the deformability of the soil column and can be estimated empirically or calculated numerically through a local seismic response analysis. In this calculation, if remediation actions have to be implemented, the effects of ground improvement should be taken into account considering their effect in terms of stiffness increase.

Figure 6.3 summarizes the steps necessary to calculate FS(z) with the semi-empirical stress-based approach (Boulanger and Idriss, 2014; Idriss and Boulanger, 2008).

It has to be highlighted that, even though the normalized values q_{c1Ncs} and $(N_1)_{60cs}$ take into account the fines content, sometimes they may lead to a misprediction of soil capacity: this is for instance the case of pyroclastic soils, which may have a relevant fines content FC with no plasticity (which means that the normalized resistance overestimates the beneficial effect of FC on CRR), and their fragile grains may be easily crushed by the testing tool (especially during SPT) (which means that soil shear strength may be underestimated). The combined effect of these two peculiarities cannot be theoretically assessed, but some experimental evidence (i.e., Anderson et al. (2019)) indicate that the use of the semi-empirical stress-based approach for pyroclastic soils is largely conservative, because of an overall underestimate of soil capacity.

Moreover, it should be stressed that the simplified approach just described does not consider peculiar site mechanisms that may affect the overall behaviour, like for instance the so called "system response" in layered deposits, smartly identified by Cubrinovski et al. (2019) in well documented case histories in Christchurch.

$$q_{c1} = C_N \cdot q_c$$

$$q_{c1N} = \frac{q_{c1}}{P_a} \quad (P_a = 101kPa)$$

$$C_N = \left(\frac{P_a}{\sigma'_v}\right)^m \leq 1.7 \quad m = 1.338 - 0.249 \cdot (q_{c1N})^{0.264}$$

$$(N_1)_{60} = C_N \cdot N_{60}$$

$$C_N = \left(\frac{P_a}{\sigma'_v}\right)^m \leq 1.7 \quad m = 0.784 - 0.0768 \cdot \sqrt{(N_1)_{60cs}}$$

$$FC = 80 \cdot (I_c + C_{FC}) - 137 \quad -0.29 \leq C_{FC} \leq 0.29$$

$$I_c = \left[(3.47 - logQ)^2 + (1.22 + logF)^2\right]^{0.5} \quad \begin{cases} Q = \left(\frac{q_c - \sigma_{vc}}{P_a}\right) \cdot \left(\frac{P_a}{\sigma'_{vc}}\right)^n \\ F = \left(\frac{f_s}{q_c - \sigma_{vc}}\right) \cdot 100 \end{cases}$$

$$FC = 80 \cdot (I_c + C_{FC}) - 137 \quad -0.29 \leq C_{FC} \leq 0.29$$

$$I_c = -0.717 \cdot ln\left(\frac{V_s^2}{9.81 \cdot z}\right) + 6.3211 \quad \begin{cases} V_s = 100.59 \cdot N_{SPT}^{0.302} \end{cases}$$

$$\Delta q_{c1N} = \left(11.9 + \frac{q_{c1N}}{14.6}\right) \cdot exp\left[1.63 - \frac{9.7}{FC + 2} - \left(\frac{15.7}{FC + 2}\right)^2\right]$$

$$q_{c1Ncs} = q_{c1N} + \Delta q_{c1N}$$

$$\Delta(N_1)_{60} = exp\left[1.63 + \frac{9.7}{FC + 0.01} - \left(\frac{15.7}{FC + 0.01}\right)^2\right]$$

$$(N_1)_{60cs} = (N_1)_{60} \quad \Delta(N_1)_{60}$$

$$CRR_{M=7.5,\sigma'v=1} = \exp\left[\frac{q_{c1Ncs}}{113} + \left(\frac{q_{c1Ncs}}{1000}\right)^2 - \left(\frac{q_{c1Ncs}}{140}\right)^3 + \left(\frac{q_{c1Ncs}}{137}\right)^4 - 2.8\right]$$

$$CRR_{M=7.5,\sigma'v=1} = \exp\left[\frac{(N_1)_{60cs}}{14.1} + \left(\frac{(N_1)_{60cs}}{126}\right)^2 - \left(\frac{(N_1)_{60cs}}{23.6}\right)^3 + \left(\frac{(N_1)_{60cs}}{25.4}\right)^4 - 2.8\right]$$

$$FS = \frac{CRR}{CSR}$$

$$CSR = 0.65 \cdot \frac{a_{max}}{g} \cdot \frac{\sigma_v}{\sigma'_v} \cdot r_d \cdot \frac{1}{MSF} \cdot \frac{1}{K_\sigma} \cdot \frac{1}{K_\alpha}$$

$$\ln(r_d) = \alpha + \beta \cdot M \quad \begin{cases} \alpha = -1.012 - 1.26 \cdot sen\left(\frac{z}{11.73} + 5.133\right) \\ \beta = 0.106 - 0.118 \cdot sen\left(\frac{z}{11.28} + 5.142\right) \end{cases}$$

$$C_\sigma = \frac{1}{37.3 - 8.27 \cdot q_{c1Ncs}^{0.264}} \leq 0.3 \qquad K_\sigma = 1 - C_\sigma \cdot ln\frac{\sigma'_v}{P_a} \leq 1.1 \qquad C_\sigma = \frac{1}{18.9 - 2.55 \cdot (N_1)_{60cs}^{0.5}} \leq 0.3$$

$$MSF = 6.9 \cdot exp\left(-\frac{M}{4}\right) - 0.058$$

$$K_\alpha = a + b \cdot exp\left(-\frac{\xi_R}{c}\right) \quad \begin{cases} a = 1267 + 636 \cdot \alpha^2 - 634 \cdot \exp(\alpha) - 632 \cdot \exp(-\alpha) \\ b = \exp(-1.11 + 12.3 \cdot \alpha^2 + 1.31 \cdot ln(\alpha + 0.0001)) \\ c = 0.138 + 0.126 \cdot \alpha + 2.52 \cdot \alpha^3 \end{cases} \quad \alpha = \frac{\tau_s}{\sigma'_{vc}}$$

$$\xi_R = \frac{1}{Q - ln\left[\frac{100 \cdot (1 + 2 \cdot K_0) \cdot \sigma'_{vc}}{3 \cdot P_a}\right]} - (0.478 \cdot q_{c1Ncs}^{0.264} - 1.063) \qquad \xi_R = \frac{1}{Q - ln\left[\frac{100 \cdot (1 + 2 \cdot K_0) \cdot \sigma'_{vc}}{3 \cdot P_a}\right]} - \sqrt{\frac{(N_1)_{60}}{46}}$$

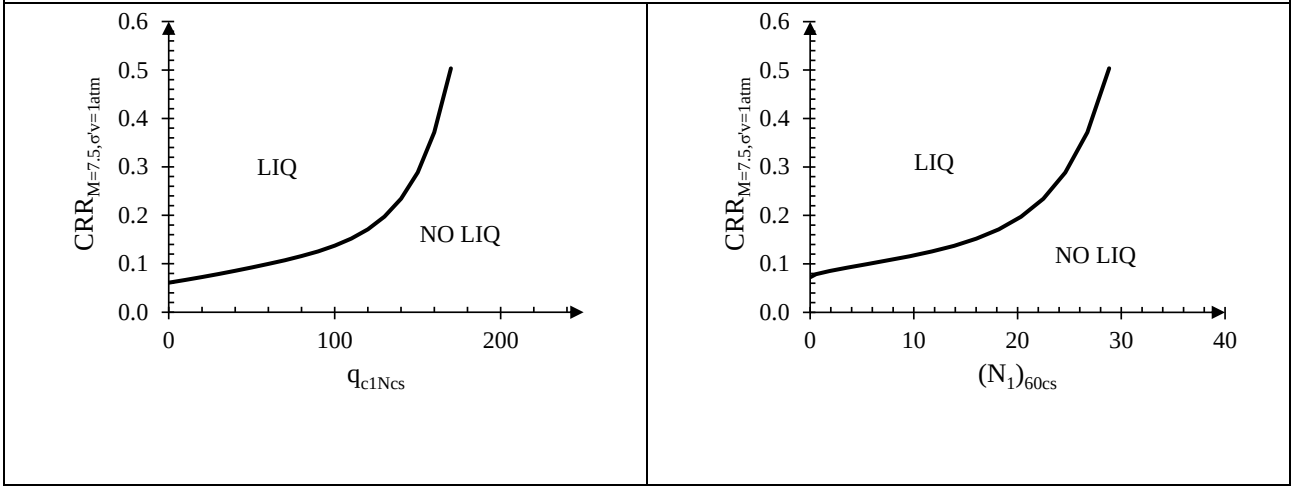

Figure 6-3. Procedure to calculate FS(z) based on the knowledge of (a) qc1Ncs or (b) (N1)60cs.

This mechanism, that can be quantitatively taken into account only using fully coupled advanced dynamic analyses, is related to the hydraulic interaction between contiguous granular layers, i.e., to the change in their pore pressure regime during the earthquake (or immediately after it) caused by transient inter-layer flows that may lead to the liquefaction of layers initially far from it.

FS values lower than 1 imply the liquefaction susceptibility of site. In this case, the potential consequences of liquefaction can be evaluated with the integral response of the deposit, through the simplified liquefaction index LSN (Tonkin and Taylor, 2012), defined as:

$$LSN = 1000 \int_0^{20} \frac{\varepsilon_v}{z} dz \qquad Eq.\ 5$$

where z is the depth in meters and ε_v is the post-liquefaction volumetric reconsolidation strain (entered as a decimal) that can be calculated according to existing charts (see (Ishihara and Yoshimine, 1992). Degree of damage can be estimated as:

- 0<LSN<20: minor;
- 20<LSN<40: major;
- LSN>40: severe.

It is worth mentioning that LSN is not the only indicator proposed in literature, and many alternatives have been suggested in time. From a historical point of view, the first (and most popular) integral indicator is the *Liquefaction Potential Index, LPI* (Iwasaki et al., 1984), which represents a measure of the vulnerability of a site as a single value, ranging between 0 (very low risk) and values over 15 (very high risk), defined as:

$$LPI = \int_0^{20} F(z) \cdot W(z) dz \qquad Eq.\ 6$$

where z is the depth in meters, while $F(z)$ and $W(z)$ are respectively:

$$F(z) = \{1 - FS \quad for \quad FS \quad < 1\ 0 \qquad for \quad FS \quad \geq 1 \qquad Eq.\ 7$$

$$W(z) = 10 - 0.5z \qquad Eq.\ 8$$

in which FS is computed by *Eq. 1*.

6.2.2 Settlements assessment

In sandy soil deposits, the effective stresses may approach zero and consequently the soil behaviour switches from that of a solid to that of a fluid. Such a phenomenon is known as liquefaction. If the liquefaction phenomenon is attained, relevant vertical settlements of shallow-founded buildings and other engineering facilities occur. In many recent strong earthquakes (e.g., New Zealand, 2011; Japan, 2011; Emilia Romagna, 2012; Turkey, 2023) the liquefaction induced settlements have resulted in significant damages on the built environment.

In practice the seismic induced building settlements are quantified via empirical procedures that were developed considering the one dimensional (1-D) volumetric consolidation settlements in "free-field" conditions, neglecting the presence of the structure at the ground level (e.g., Ishihara and Yoshimine, 1992; Tokimatsu and Seed, 1987). In other words, only the volumetric strains, mainly due to the dissipation of the excess pore water pressure accumulated during the seismic sequence, are considered.

Settlements (w) can be estimated by the following equation:

$$w = \sum_{i=1}^{j} \varepsilon_{z,i} \cdot \Delta z_i \qquad Eq.\ 9$$

where ε_{zi} is the post-liquefaction volumetric strain for the soil sublayer i; Δ_{zi} is the thickness of the sublayer i; and j is the number of soil sublayers.

Methods to estimate liquefaction-induced settlements aim to predict how much the ground will subside due to soil liquefaction during seismic events. These methods primarily focus on the behaviour of loose, saturated soils (often sands and silts) that lose strength when shaken. The approaches for liquefaction-induced settlements vary from simple empirical approaches, which are based on field test data and past experiences,

to more complex numerical models that simulate soil behaviour under seismic conditions. Empirical methods are easy to apply but may lack precision in diverse geotechnical conditions, while analytical, stress-strain, and probabilistic methods offer greater accuracy but require more detailed input data and computational resources. The choice of method depends on the complexity of the site conditions, the availability of data, and the level of precision required for the engineering analysis. Here are the most common methods used for estimating liquefaction-induced settlements.

Stress-strain methods involve the use of constitutive models that simulate soil behaviour under seismic loading. These models attempt to represent the complex interactions between stress, strain, and pore water pressure in soils during liquefaction. Numerical methods, such as finite element analysis (FEA), are typically used to solve these models. Examples include Finite Element Modelling (FEM) and Plasticity Models. In the Finite Element Modelling (FEM) advanced numerical simulations use constitutive models for soils, such as the Mohr-Coulomb or more sophisticated cyclic models, to simulate the liquefaction process and resulting ground settlements. Plasticity Models focus on the plastic deformation of soils and incorporate parameters like yield strength, post-yield stiffness, and pore pressure development to estimate liquefaction-induced settlements. Models like the UBCSAND model (University of British Columbia Sand Model) are used in numerical simulations for liquefaction analysis.

Probabilistic methods incorporate uncertainty and variability in soil properties, seismic loading, and site conditions. They provide estimates of liquefaction-induced settlements based on probability distributions rather than deterministic values. These methods are useful in risk-based assessments and help account for the variability in seismic and soil parameters. Monte Carlo Simulations uses statistical methods to generate numerous possible outcomes of liquefaction and settlement based on variable inputs (e.g., soil density, seismic intensity). Results are presented in terms of probability distributions of settlements. Probabilistic Seismic Hazard Analysis (PSHA), often coupled with Monte Carlo methods, PSHA helps to account for the variability and uncertainties in earthquake characteristics and their impacts on liquefaction-induced settlements.

Semi-empirical models combine elements of both empirical correlations and mechanistic understanding of soil behaviour. These models are developed by integrating case histories with theoretical considerations, providing a balance between simplified methods and more complex numerical models.

Empirical approaches rely on correlations derived from case histories of liquefaction events and field test data. These methods use simplified parameters to estimate settlements based on past experiences. These methods are relatively simple and easy to apply but can sometimes be limited by their reliance on specific case studies and conditions. Common empirical methods include:

- Tokimatsu and Seed (1987): This widely used method relates the Standard Penetration Test (SPT) or Cone Penetration Test (CPT) results with the amount of post-liquefaction settlement. It involves determining the factor of safety against liquefaction and using empirical curves to estimate settlements based on soil density and cyclic stress ratio (CSR).
- Ishihara and Yoshimine (1992): This method provides an empirical relationship between the liquefaction-induced vertical strain and the factor of safety against liquefaction, with settlement being calculated by multiplying vertical strain by the thickness of liquefied layers.

Simplified Analytical Methods use a combination of empirical correlations and analytical equations to estimate settlements. They often involve calculating the cyclic stress ratio (CSR) and comparing it with the cyclic resistance ratio (CRR) of the soil to estimate liquefaction triggering. Once triggering is assessed, settlements are estimated using strain-based or volumetric deformation models. Examples include:

- Idriss and Boulanger (2008): This method refines earlier empirical methods by incorporating updated seismic hazard data and soil characteristics, and it provides more detailed guidelines for estimating liquefaction triggering and resulting ground deformation.
- Zhang et al. (2002): This CPT-based method estimates post-liquefaction settlements using cone tip resistance to assess the liquefaction potential and corresponding settlements in each soil layer. They linked the volumetric strains induced by the dissipation of the excess pore water pressure to FS and qc1Ncs (results of CPT tests) as shown in Figure 6.4.

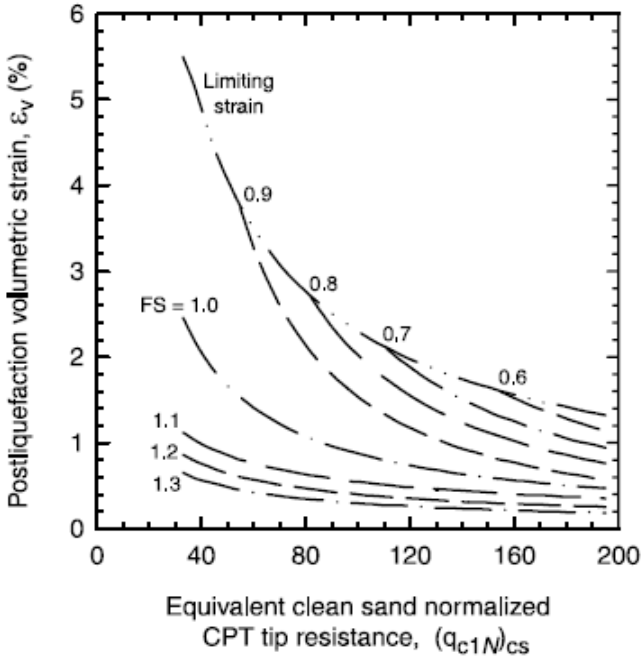

Figure 6-4. Relationship between post-liquefaction volumetric strain and equivalent clean sand normalized CPT tip resistance for different factors of safety (FS).

The equations are reported below:

$$if\ FS \leq 0.5,\quad \varepsilon_v = 102 \cdot (q_{c1ncs})^{-0.82} \quad for\ 33 \leq q_{c1ncs} \leq 200$$

$$if\ FS = 0.6,\quad \varepsilon_v = 102 \cdot (q_{c1ncs})^{-0.82} \quad for\ 33 \leq q_{c1ncs} \leq 147$$

$$if\ FS = 0.6,\quad \varepsilon_v = 2411 \cdot (q_{c1ncs})^{-1.45} \quad for\ 147 \leq q_{c1ncs} \leq 200$$

$$if\ FS = 0.7,\quad \varepsilon_v = 102 \cdot (q_{c1ncs})^{-0.82} \quad for\ 33 \leq q_{c1ncs} \leq 110$$

$$if\ FS = 0.7,\quad \varepsilon_v = 1701 \cdot (q_{c1ncs})^{-1.42} \quad for\ 110 \leq q_{c1ncs} \leq 200$$

$$if\ FS = 0.8,\quad \varepsilon_v = 102 \cdot (q_{c1ncs})^{-0.82} \quad for\ 33 \leq q_{c1ncs} \leq 80$$

$$if\ FS = 0.8,\quad \varepsilon_v = 1690 \cdot (q_{c1ncs})^{-1.46} \quad for\ 80 \leq q_{c1ncs} \leq 200$$

$$if\ FS = 0.9,\quad \varepsilon_v = 102 \cdot (q_{c1ncs})^{-0.82} \quad for\ 33 \leq q_{c1ncs} \leq 60$$

$$if\ FS = 0.9,\quad \varepsilon_v = 1430 \cdot (q_{c1ncs})^{-1.48} \quad for\ 60 \leq q_{c1ncs} \leq 200$$

$$if\ FS = 1.0,\quad \varepsilon_v = 64 \cdot (q_{c1ncs})^{-0.93} \quad for\ 33 \leq q_{c1ncs} \leq 200$$

$$if\ FS = 1.1,\quad \varepsilon_v = 11 \cdot (q_{c1ncs})^{-0.65} \quad for\ 33 \leq q_{c1ncs} \leq 200$$

$$if\ FS = 1.2,\quad \varepsilon_v = 9.7 \cdot (q_{c1ncs})^{-0.69} \quad for\ 33 \leq q_{c1ncs} \leq 200$$

$$if\ FS = 1.3,\quad \varepsilon_v = 7.6 \cdot (q_{c1ncs})^{-0.71} \quad for\ 33 \leq q_{c1ncs} \leq 200$$

$$if\ FS = 2.0,\quad \varepsilon_v = 0 \quad for\ 33 \leq q_{c1ncs} \leq 20$$

In the development of the Project the settlements will be evaluate by CPT-based method.

6.2.3 Uncertainties in Liquefaction Assessment

The methods used to assess liquefaction susceptibility involve a range of uncertainties due to various factors inherent in the geotechnical processes, data collection, and modelling approaches. These uncertainties can influence the accuracy and reliability of predictions, potentially impacting engineering designs and risk management strategies.

One of the primary sources of uncertainty in liquefaction assessment arises from soil variability. Liquefaction potential depends on factors like soil grain size, density, water content, and stress history, which can vary significantly even within short distances at a given site. Conventional field methods, such as the Standard Penetration Test (SPT), Cone Penetration Test (CPT), and laboratory tests on soil samples, often provide only localized or discrete data points. Interpolating these values across a larger area introduces uncertainty because it may not accurately represent the true heterogeneity of the subsurface materials.

Moreover, soil samples used for laboratory testing may undergo changes during extraction and transportation, leading to altered water content or density. These disturbances can result in discrepancies between in-situ soil conditions and laboratory conditions, affecting the reliability of results.

Many liquefaction assessment methods are based on empirical correlations that relate field test results (e.g., SPT or CPT data) to liquefaction susceptibility. While these empirical methods are widely used due to their simplicity and cost-effectiveness, they are typically based on datasets from specific regions or earthquake events. Applying these correlations to different geological or seismic conditions introduces uncertainty because the underlying assumptions may not hold in new environments.

For example, the widely used Seed and Idriss (1971) simplified procedure for estimating liquefaction resistance is based on empirical correlations that were developed from case histories of past earthquakes. However, these correlations may not fully capture the complexity of soil behaviour under different loading conditions, depths, or seismic events, leading to potential over- or underestimation of liquefaction potential.

The magnitude and characteristics of the seismic loading used in liquefaction assessments contribute to significant uncertainty. Liquefaction susceptibility is largely dependent on the amplitude, frequency, and duration of ground shaking during an earthquake. However, predicting the intensity and nature of future seismic events at a particular site involves inherent uncertainty due to the complex and often unpredictable nature of seismic activity. Ground motion prediction models, though useful, rely on assumptions about fault behaviour, distance from the epicentre, and regional seismicity, all of which introduce uncertainty into liquefaction assessments. Additionally, seismic loading is often characterized by the cyclic stress ratio (CSR), which quantifies the shear stresses induced by earthquake shaking. However, determining CSR involves assumptions about ground motion intensity and site-specific amplification factors, further contributing to uncertainty in liquefaction predictions.

Groundwater conditions play a critical role in liquefaction because saturated soils are more prone to this phenomenon. However, accurately determining the depth and variability of the water table is often challenging, especially in areas with seasonal fluctuations or complex hydrological conditions. Variations in water table levels can significantly influence liquefaction potential, with uncertainties in these levels leading to unreliable predictions.

In some cases, the presence of perched water tables or localized zones of high saturation may be overlooked, further increasing the uncertainty in assessing liquefaction risks. The dynamic interaction between the groundwater and soil during seismic shaking, such as pore water pressure build-up, is also difficult to predict accurately, contributing to the overall uncertainty in liquefaction analysis.

6.2.4 Liquefaction evidence in Emilia Romagna Region

In May 2012, Italy was struck by an important seismic sequence and the main shock that occurred on 20 May 2012 (Mw=6.1) caused extensive liquefaction phenomena. The epicentre of the 20 May event (44.89°N latitude and 11.23°E longitude) was located between the provinces of Modena and Ferrara, while the hypocentre was at a depth of 6.3 km, owing to that it is considered a shallow earthquake (Lai et al., 2015). Although Italy is a seismic country, liquefaction occurred only in restricted areas and owing to that the

induced damage was generally limited. The most evident effects of liquefaction phenomena following the 2012 earthquake were found in San Carlo (Municipality of Sant' Agostino) and Mirabello, whose subsoil was characterized by alluvial sediments of different depositional environments, which consists of alternated layers of silty-clayey deposits and sandy soils mainly constituting ancient rivers banks (Chiaradonna et al., 2018). After these events, the Emilia-Romagna Region and the Department of Civil Protection established an interdisciplinary working group in order to plan some investigations (boreholes, penetration tests, down holes, cross hole).

6.2.5 Data and methods

As described in section 6.2.1, the analysis for liquefaction triggering assessment of level 2 describes the parameters for the analysis (ground water table, maximum acceleration, geotechnical data). In particular CRR can be calculated from Standard Penetration Test (SPT), Cone Penetration Test (CPT) and shear wave velocity (VS) measurements. In this test area, it was calculated by CPT investigations that were obtained from the database created by the Geology, Soil, and Seismic Area of the Emilia-Romagna Region. The groundwater table depth values were obtained by interpolating the average groundwater levels from point data downloaded from the ARPAE database (Regional Agency for Prevention, Environment, and Energy of Emilia-Romagna). This data refers to the monitoring conducted from 2009 to 2022 at the underground water body stations belonging to the regional network for environmental quality. The PGA (Peak Ground Acceleration) values related to the 2012 Emilia earthquake with a magnitude of 5.8 were obtained from the INGV archive. Overall data were represented also as GIS files with a spatial location which allow them to be visualized as geographical data.

The sensitivity analysis on the approach adopted for estimating the occurrence of liquefaction was based on the investigation of the variability of two of three factors affecting the phenomena, i.e., preparatory and triggering. The first is represented by the position of the groundwater table, whose depth varies between the field level (depth = 0) and the result of an average groundwater contour map based on the monitoring carried out in the period 2009-2022 by Emilia Romagna Region.

As regards the triggering event, which is the earthquake, the method adopts the peak ground acceleration (PGA). In particular, the adopted values follow the classes of the macroseismic classification of Italy (NTC, 2008). It divides Italy into different seismic zones based on risk, classified from Zone 1 (highest risk) to Zone 4 (very low risk). Each zone corresponds to a specific PGA value:

- **Zone 1: PGA ≥ 0.25 g**
  High seismic hazard. Earthquakes can be very strong and frequent.
- **Zone 2: 0.15 g ≤ PGA < 0.25 g**
  Medium-high hazard. Earthquakes can be intense, but less frequent.
- **Zone 3: 0.05 g ≤ PGA < 0.15 g**
  Moderate hazard. Earthquakes can occur but are less intense.
- **Zone 4: PGA < 0.05 g**
  Low seismic hazard. Earthquakes are rare and of low intensity.

For sake of simplicity the investigated values pertain to the Zone 1 and Zone 2, as this process requires a high energetic earthquake for triggering. Hence, the proposed analysis of the Liquefaction Potential Index (LPI) was carried out following four scenarios:

Scenario 1:

- Water table: mean value of depth data from 2009 to 2022
- PGA: 0.15 g

Scenario 2:

- Water table: mean value of depth data from 2009 to 2022
- PGA: 0.25 g

Scenario 3:

- Water table: 0
- PGA: 0.15 g

Scenario 4:

- Water table: 0
- PGA: 0.25 g

6.2.6 Looking for uncertainties: Sensitivity analysis

Sensitivity analysis was conducted in order to investigate the variability of the outputs on both the processed CPT dataset and their spatial distribution. In the first case, the investigated CPTs were used to calculate the Liquefaction Potential Index, LPI (Iwasaki et al., 1984) for each scenario and then a statistical analysis was conducted on the output data. In the second case, a reference computation grid was created based on the location of the investigations and statistical analysis was performed on each grid cell to assess the spatial variability of the data.

In particular, the main statistical variables were calculated: maximum, minimum, median, average standard deviation and variance value then descriptive graphs were drawn up.

6.2.7 Looking for uncertainties: Variability of Dataset

In the study area, 2035 CPTs are available, and the depth of the groundwater table was calculated for each one. Afterward, using a macro developed in an excel spreadsheet, it was possible to evaluate for some of them (with a semi-automatic method) the factor of safety (FS) at each depth and the representative LPI for the entire vertical. 203 CPTs have been processed until now, of which 131 were representative of liquefiable sandy layers, 72 were located in areas with no sandy layers and therefore not suitable for liquefaction assessment.

In Figure 6.5 an example of a processed CPT with the representation of liquefiable and non-liquefiable layers and the variation of the FS along the vertical z is shown.

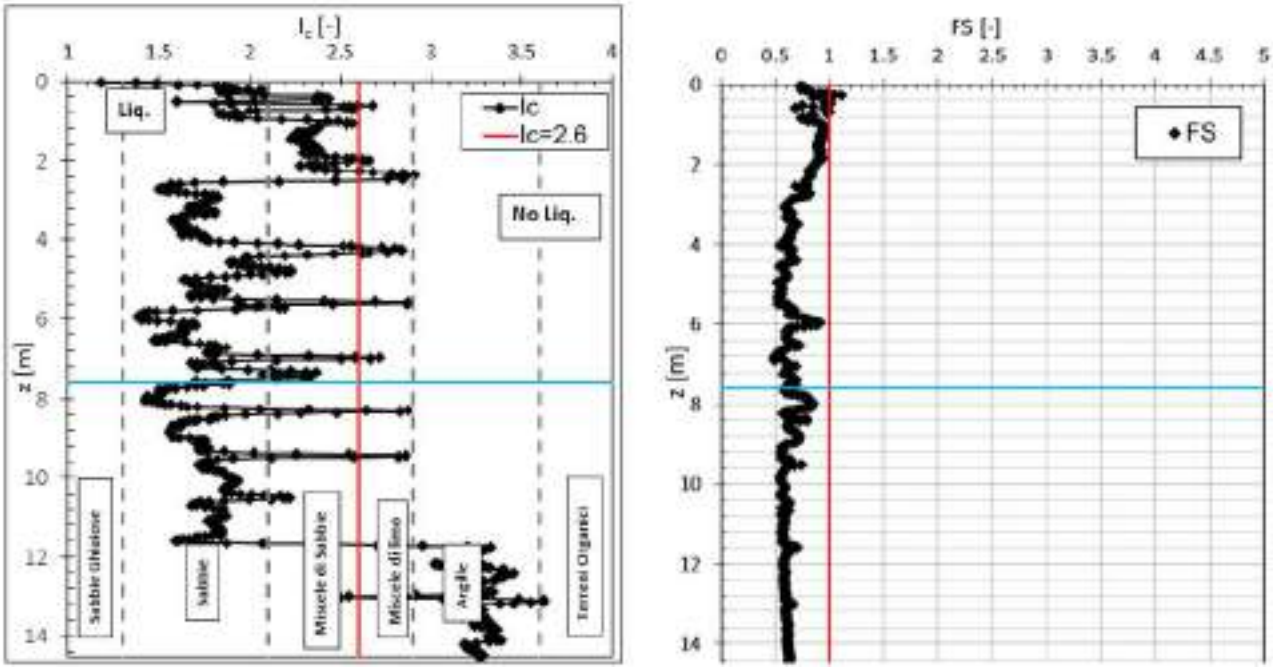

Figure 6-5. Representation of liquefiable and non-liquefiable layers and the variation of the FS along the vertical z.

Figure 6.6 shows the spatial distribution of the entire dataset of CPTs available in the test area. The blue dots indicate those not suitable for liquefaction estimation because localized in areas with a stratigraphic sequence characterised mainly by clayey levels, with thin or without sandy layers. The green dots indicate the CPTs processed because localized in areas with potentially liquefiable sandy layers. Finally, the grey dots indicate CPTs that will be processed successively.

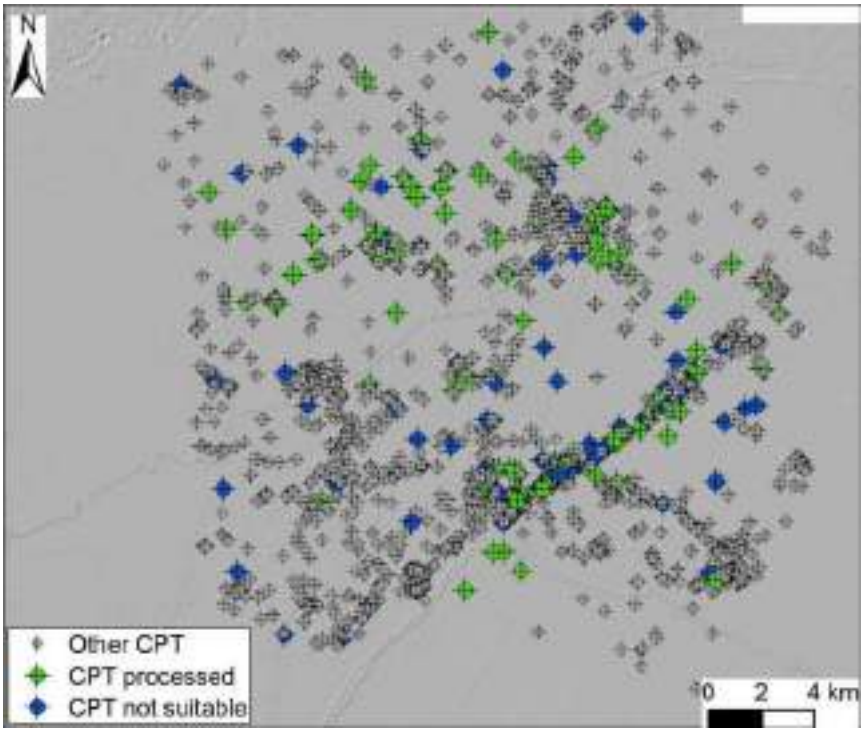

Figure 6-6. Spatial distribution of CPT data available in the test area with highlights of processed and not suitable for liquefaction assessment

The potential liquefaction index, LPI, was also calculated for each investigation according to *Eq. 6* by changing both the value of the preparatory factor (groundwater) and the value of the trigger (PGA) according to the four scenarios described in section 6.2.5. Figure 6.7 shows the spatial distribution of the LPI values for each scenario (IL). It shows that by moving from scenario 1 (IL_1) to scenario 4 (IL_4), the severe conditions increase, as the groundwater depth goes to zero (IL_3 and IL_4) or the value of peak ground acceleration (PGA) increases (IL_2 and IL_4).

Figure 6.8 shows the statistics of LPI and a boxplot for each scenario. It can be how the variability of data changes passing from scenario 1 to scenario 4 increasing. The standard deviation, indeed, increase from 3.3 to 10.5. IL_2 and IL_3 are similar in terms of distribution and variability.

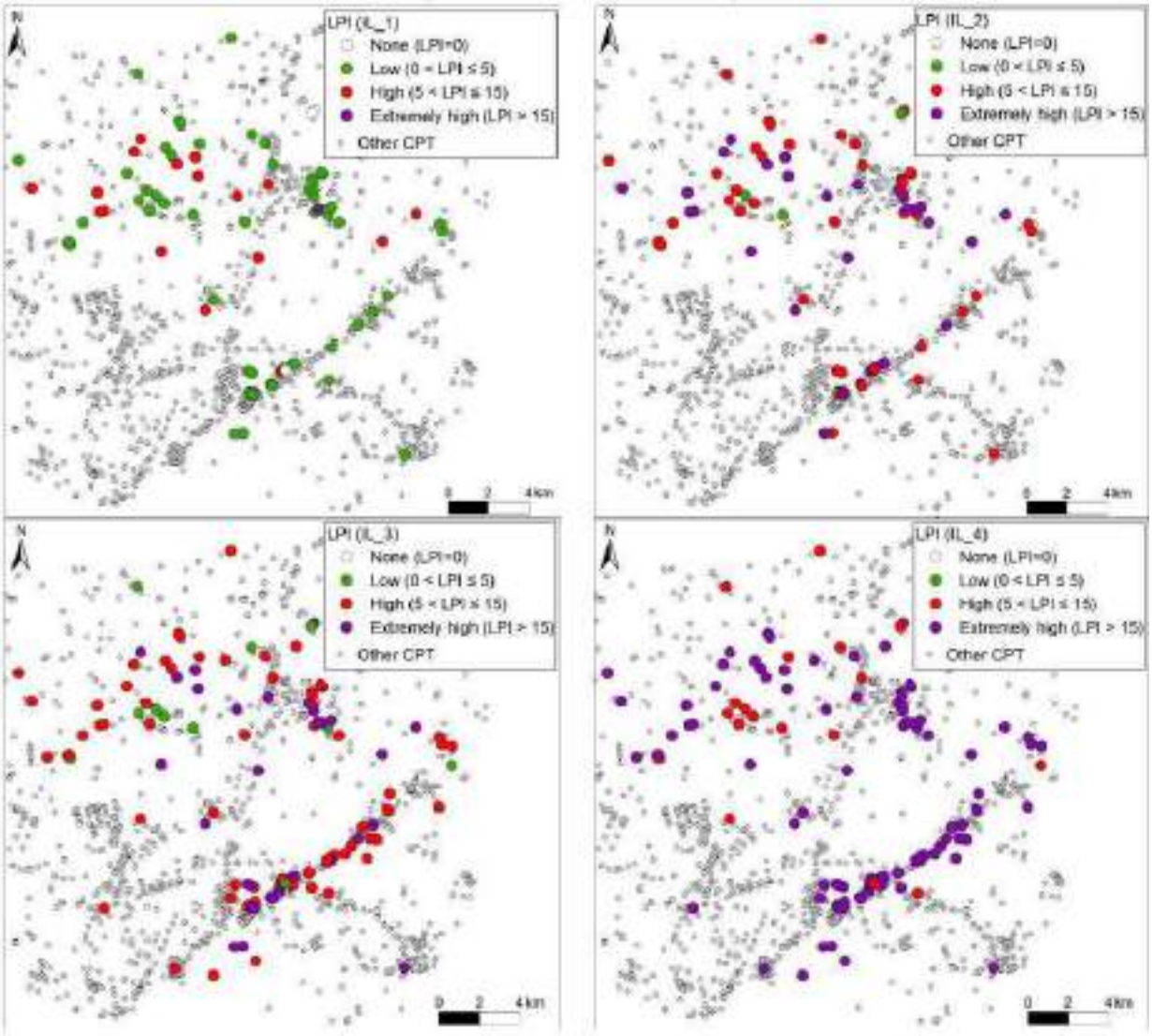

Figure 6-7. Spatial distribution of Liquefaction potential index (LPI) for each scenario

Statistic	IL_1	IL_2	IL_3	IL_4
N. of observations	131	131	131	131
Minimum	0.0	1.8	1.3	6.1
Maximum	17.0	41.0	38.7	58.1
1st Quartile	0.6	8.8	8.8	17.1
Median	1.2	11.7	12.3	22.5
3rd Quartile	4.3	18.5	18.3	31.7
Mean	2.8	14.0	14.2	24.8
Variance	10.9	56.5	67.1	111.2
Standard deviation	3.3	7.5	8.2	10.5

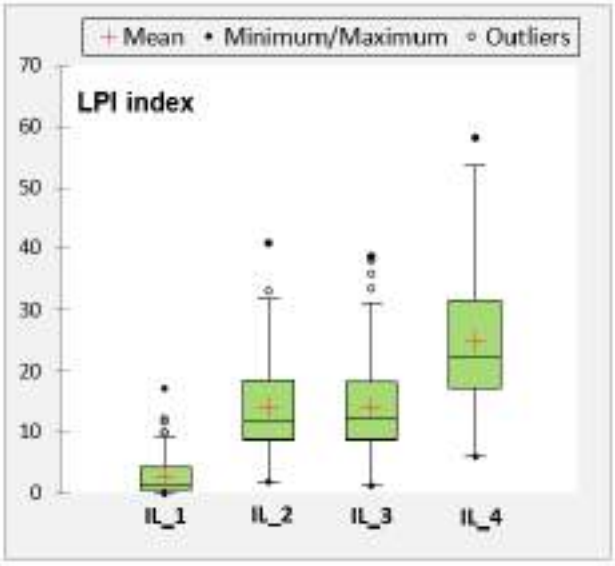

Figure 6-8. Statistics and boxplot of LPI

The charts in Figure 6.9 shows the distribution of LPI classes for each scenario. IL_1 graph shows that most observations fall into the "low" category, with around 70% of occurrences. Fewer observations are found in the "high" category, while the "very high" category shows almost no occurrences, suggesting that a high potential liquefaction is rare for IL_1. For IL_2, the distribution shifts towards higher liquefaction index values. Most observations fall into the "high" category, with nearly 40% of instances, and a significant portion also occupies the "very high" category, with around 30% of observations. These results arise from an increase value of PGA (from 0.15g to 0.25g). IL_3 and IL_4 show a clear tendency towards higher levels of PLI, but with distinct patterns. IL_3 has most of its observations concentrated in the "high" category, with a significant number also falling under "very high." In contrast, IL_4 shows an even more extreme concentration in the "very high" category, where most observations are located (about 80% of occurrences).

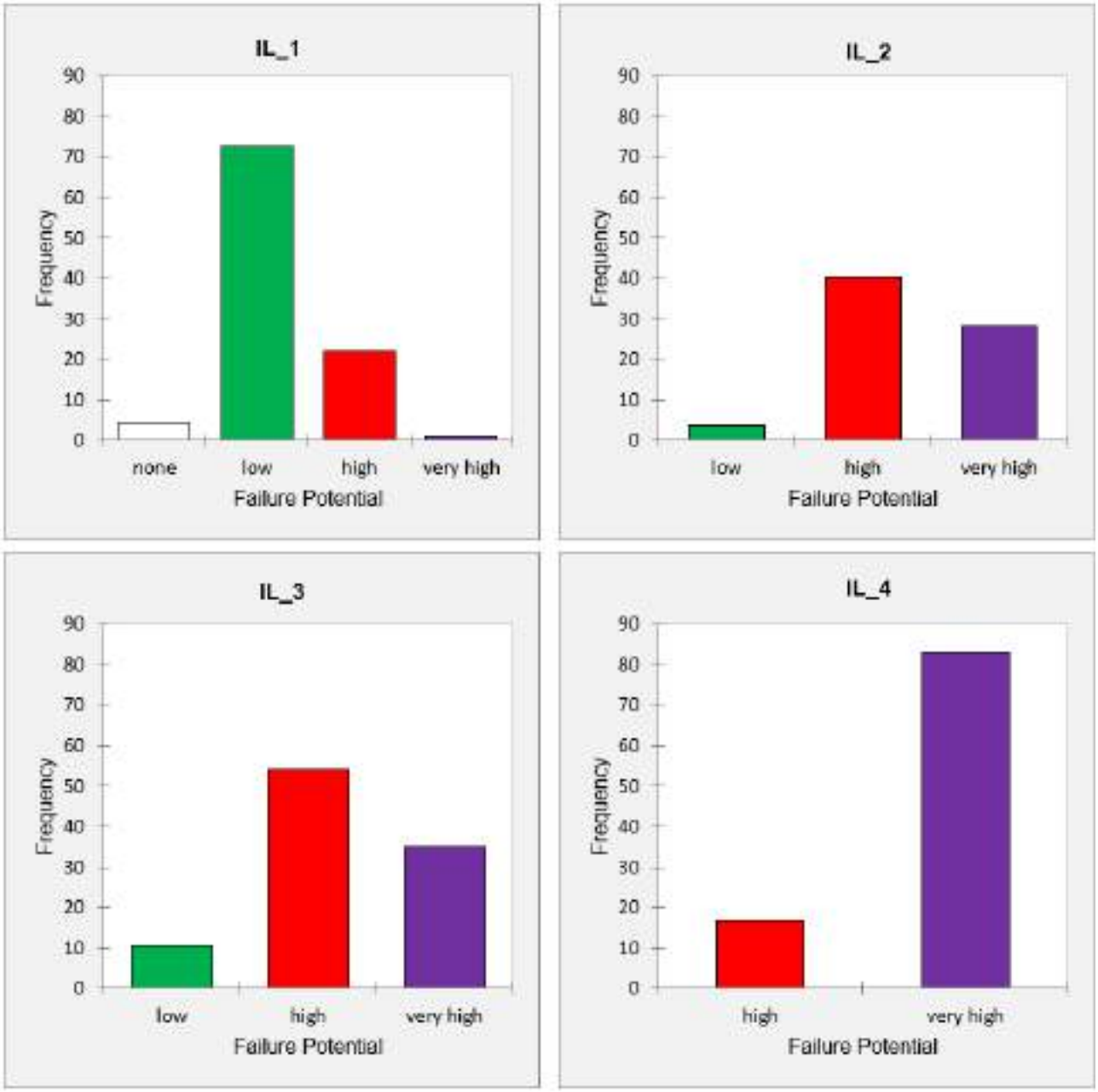

Figure 6-9. Frequency of LPI classes in each scenario

6.2.8 Variability of spatial data distribution

In order to develop a simple methodology for calculating the potential liquefaction index in a specific area, a grid-based map was proposed to assess the LPI in each cell. The size of the grid can be variable according to the size of the study area and the number of surveys available. In this case, a grid was created with cells of 2x2 km. Figure 6.10 shows the number of CPTs available and processed within each grid cell. In particular, Figure 6.10b shows that the density of the surveys is quite variable, in fact, some cells have a number of CPTs less than 15 (in the north-west area), while others have a number of surveys greater than 15. Regarding processed CPTs, on the other hand, the map shows a concentration of CPT data processing in the central areas, with higher numbers (pink and purple) and lower values (yellow and orange) in the surrounding cells Figure 6.10c.

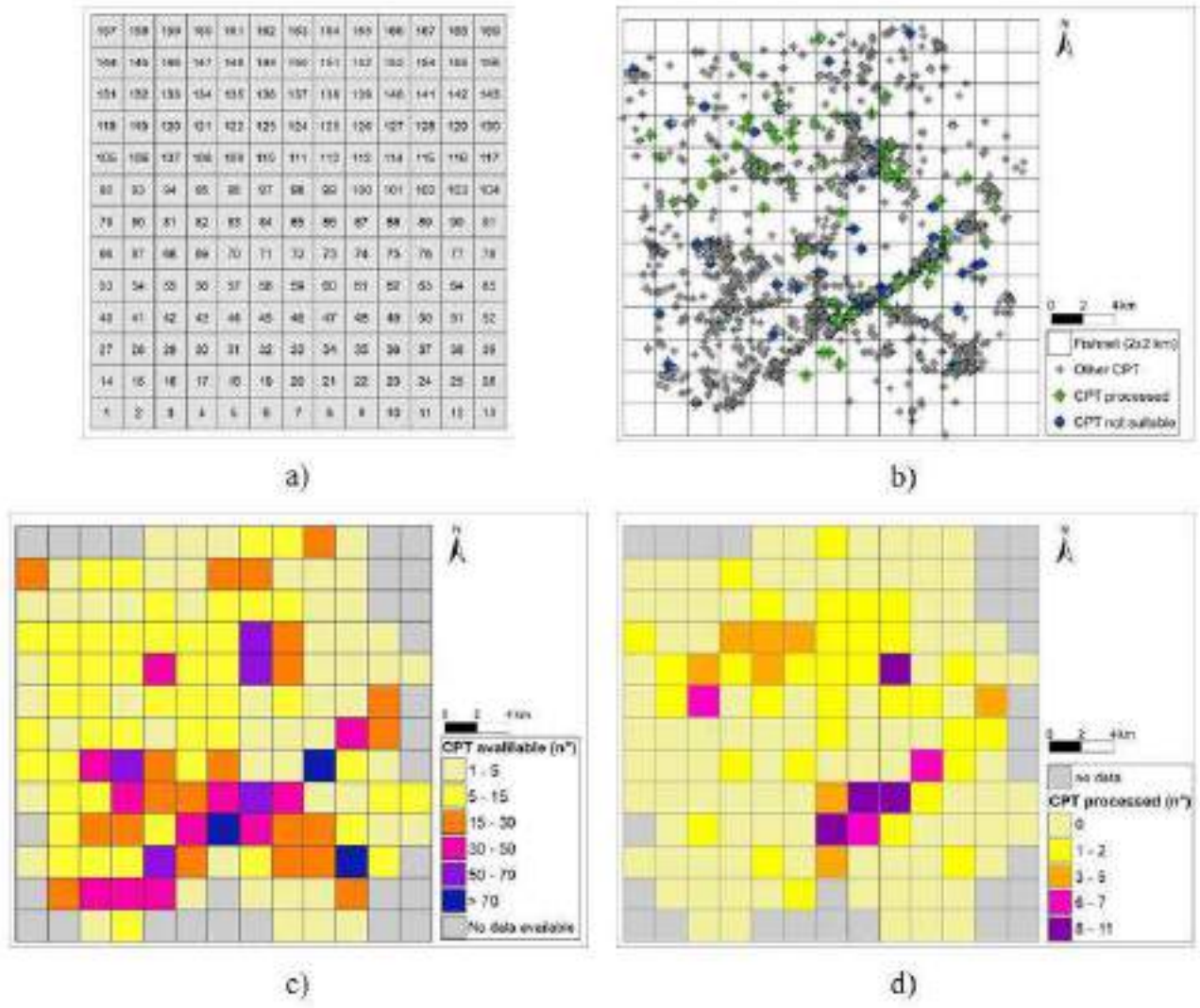

Figure 6-10. ID cell assigned (a); CPT distribution in the grid-based map (b); the number of CPT availability in each grid (c) data; the number of CPTs processed in each grid (d)

To assess the spatial variability of the LPI, minimum, maximum and average values were calculated for each liquefaction scenario (Table 6.2)

In particular, Figure 6.11 shows the distribution of the average LPI values for the four reference scenarios. Figure 6.11a shows a scattered pattern of green (low LPI values) and red (high LPI values) areas across the grid, with most of the low values concentrated towards the centre and northern parts, while high values are distributed irregularly. Some regions on the outer parts of the grid are grey, indicating a lack of data. In the map of Figure 6.11b, a significant presence of areas with high and extremely high values for scenario 2 are

present. These areas are particularly concentrated in the central and northern parts of the grid. The light green squares, representing areas with no or very low values, are scattered more sparsely across the grid.

Figure 6.11c shows several red and purple areas scattered throughout the grid, indicating a substantial presence of high and extremely high LPI values. The high (red) areas are more widely distributed, while the extremely high (purple) areas appear in specific central and southern parts. Low values (green) are less frequent, but they are clustered near the top and centre of the map. This distribution highlights the effect of the soil saturation on potential liquefaction index setting the groundwater table depth at the field level.

Finally, Figure 6.11d shows an evident increase of LPI with extremely high values most prevalent in the area, with and no low value. This distribution of high values depends on the worsening of the preparatory and trigger parameters in scenario 4, where the groundwater level is at ground level and the PGA has values of 0.25g.

Table 6.2. Statistics for each cell of grid-base map and for each scenario (the id cell is shown in Figure 6.10a)

			IL_1			IL_2			IL_3			IL_4		
ID cell	**TOT data**	**data processed**	**min**	**media**	**max**	**min**	**media**	**max**	**min**	**media**	**max**	**min**	**media**	**max**
19	1	1							13.6	13.6	13.6	18.2	18.2	18.2
31	54	1							10.0	10.0	10.0	16.5	16.5	16.5
33	4	3	2.2	2.9	3.5	13.7	16.8	19.9	12.3	20.5	26.9	21.0	28.7	35.3
37	84	1	0.3	0.3	0.3	10.5	10.5	10.5	15.3	15.3	15.3	27.1	27.1	27.1
42	20	1							11.1	11.1	11.1	21.0	21.0	21.0
46	115	10	0.3	1.3	2.9	4.1	11.5	19.2	6.2	17.5	30.5	15.5	29.1	41.5
47	39	7	0.0	2.2	9.9	9.6	18.3	33.2	13.4	22.8	38.7	27.0	35.8	53.6
48	30	1	0.2	0.2	0.2	6.2	6.2	6.2	7.1	7.1	7.1	11.9	11.9	11.9
59	32	5	0.4	0.8	1.0	9.4	11.0	12.3	10.2	14.4	17.2	17.0	22.8	26.2
60	60	11	0.0	3.0	8.6	5.2	18.1	25.0	3.3	20.4	36.1	10.3	31.5	49.9
61	40	9	0.2	0.2	0.2	13.6	13.6	13.6	7.5	13.9	20.6	17.6	24.9	37.9
62	1	1							10.9	10.9	10.9	15.2	15.2	15.2
69	52	1							5.2	5.2	5.2	12.1	12.1	12.1
71	14	2	1.2	3.2	5.2	10.3	13.3	16.4	7.7	16.5	25.3	16.2	24.3	32.5
75	101	7	1.0	2.0	3.1	10.8	13.7	16.7	10.0	14.9	27.4	17.7	24.8	36.8
76	10	1							8.9	8.9	8.9	18.9	18.9	18.9
85	11	1	6.4	6.4	6.4	18.4	18.4	18.4	22.2	22.2	22.2	32.0	32.0	32.0
89	37	2	0.1	0.1	0.1	8.7	8.7	8.7	9.2	11.1	13.1	17.2	19.4	21.5
90	21	1							13.7	13.7	13.7	27.5	27.5	27.5
93	11	1							14.5	14.5	14.5	19.1	19.1	19.1
94	11	6	1.0	1.7	4.3	8.8	10.2	11.8	3.9	6.7	11.8	11.9	15.6	21.0
96	12	1	5.0	5.0	5.0	18.1	18.1	18.1	20.6	20.6	20.6	32.2	32.2	32.2
98	13	1	1.1	1.1	1.1	5.7	5.7	5.7	7.9	7.9	7.9	14.8	14.8	14.8
100	13	1	3.6	3.6	3.6	20.5	20.5	20.5	9.5	9.5	9.5	33.4	33.4	33.4
101	5	1	11.5	11.5	11.5	27.9	27.9	27.9	28.0	28.0	28.0	45.5	45.5	45.5
103	27	4	0.1	1.1	2.0	9.6	10.4	11.3	4.8	8.9	11.8	11.0	18.6	22.4
106	6	1	6.7	6.7	6.7	15.5	15.5	15.5	11.1	11.1	11.1	18.8	18.8	18.8
107	8	4	5.9	7.8	9.1	16.7	21.0	25.9	9.4	12.8	14.9	19.7	25.2	30.4
108	15	1	1.2	1.2	1.2	7.0	7.0	7.0	4.3	4.3	4.3	14.1	14.1	14.1
109	37	4	0.4	1.1	1.8	3.8	6.1	7.4	1.3	4.5	7.8	6.9	10.3	13.6
110	9	2	0.7	3.8	6.8	3.9	11.2	18.6	2.4	10.8	19.1	6.1	17.6	29.1
111	11	1	10.0	10.0	10.0	25.3	25.3	25.3	22.7	22.7	22.7	36.1	36.1	36.1
112	54	1	5.6	5.6	5.6	17.1	17.1	17.1	17.6	17.6	17.6	27.3	27.3	27.3
113	30	10	0.1	3.7	17.0	8.2	18.1	41.0	4.7	15.9	38.2	15.5	31.3	58.1
115	4	1	5.8	5.8	5.8	17.7	17.7	17.7	18.1	18.1	18.1	28.8	28.8	28.8
118	7	1	2.6	2.6	2.6	12.9	12.9	12.9	6.4	6.4	6.4	19.6	19.6	19.6
121	8	3	2.1	5.1	7.5	9.0	15.7	19.6	8.8	13.2	20.6	15.7	23.3	31.5
122	7	4	0.1	3.4	11.9	4.9	12.1	27.8	5.5	13.9	30.4	10.4	22.8	44.6
123	10	4	0.7	4.3	6.4	7.6	23.4	31.8	5.1	18.1	31.2	14.2	32.6	51.2
124	11	1	0.8	0.8	0.8	7.6	7.6	7.6	7.6	7.6	7.6	18.3	18.3	18.3
125	53	1	1.6	1.6	1.6	8.8	8.8	8.8	6.0	6.0	6.0	14.0	14.0	14.0
126	17	2	0.9	1.4	1.8	8.0	11.2	14.4	13.2	15.8	18.4	21.6	26.6	31.6

135	15	2	0.2	0.7	1.2	11.5	11.6	11.7	7.4	8.8	10.2	18.8	21.2	23.6
137	6	1	0.1	0.1	0.1	6.3	6.3	6.3	4.3	4.3	4.3	11.9	11.9	11.9
138	8	1							13.8	13.8	13.8	20.1	20.1	20.1
139	7	2	0.0	0.0	0.0	1.8	4.4	6.9	2.2	8.9	15.5	14.7	23.8	32.9
147	10	2	0.4	0.7	1.0	5.4	5.7	6.1	1.8	2.4	3.1	8.7	10.1	11.5
163	3	1	0.8	0.8	0.8	6.0	6.0	6.0	9.7	9.7	9.7	14.3	14.3	14.3

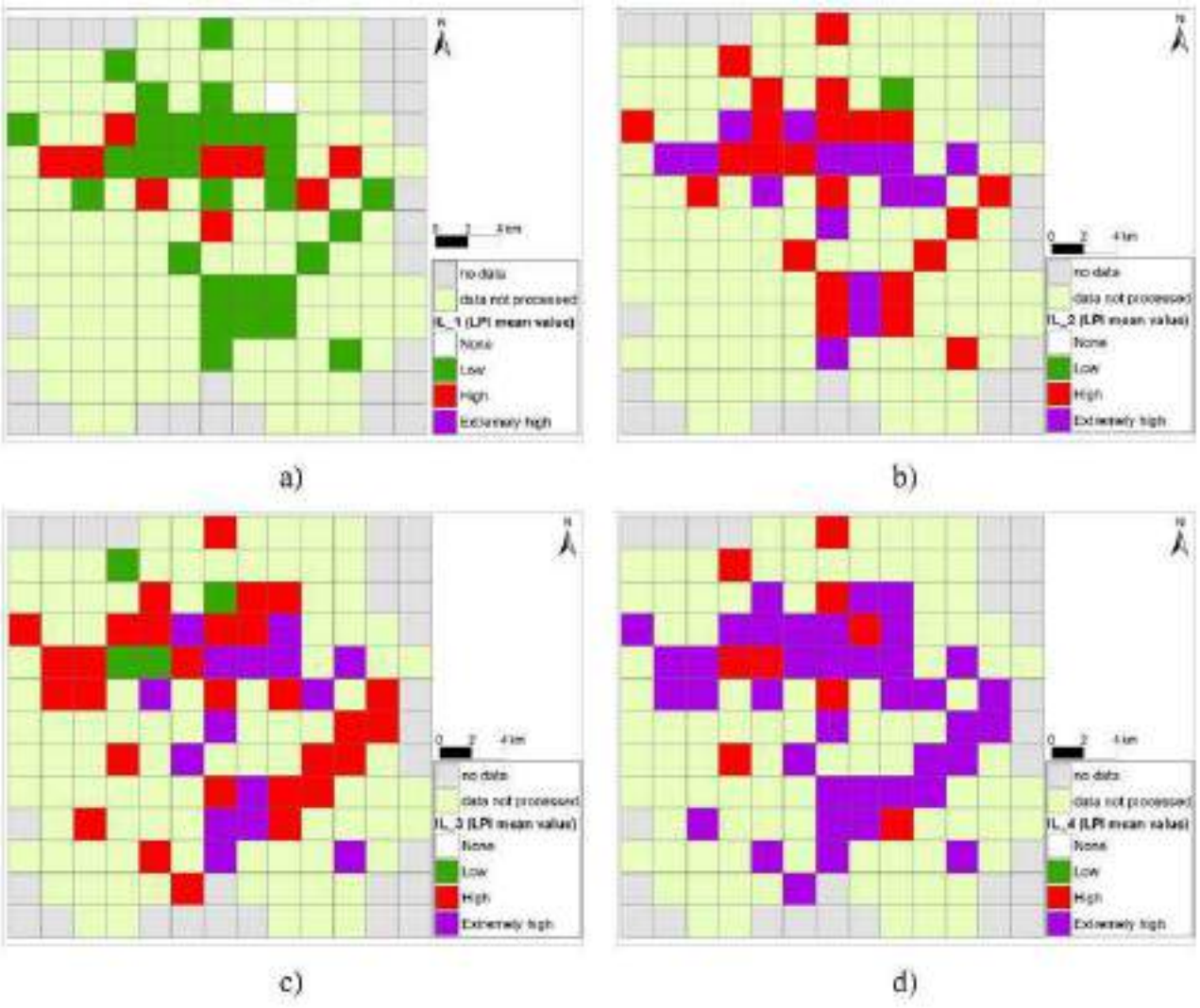

Figure 6-11. Spatial distribution of LPI average value for a) scenario 1; b) scenario 2; c) scenario 3; d) scenario 4

6.3 Discussion and Conclusions

The assessment of uncertainty related to the study of natural phenomena is complex due to the large number of factors that are involved and their variability associated with each of them.

The uncertainty assessment was carried out on two input data related to the liquefaction phenomenon, the depth of the water table, considered as a preparatory factor, and the peak ground acceleration (PGA), considered as a triggering factor. In particular, the variability of the liquefaction potential index (LPI) was analysed by changing both factors and thus developing 4 reference scenarios, in order to understand the impact of each on the phenomenon considered. The analysis conducted on the average LPI values showed a clear correlation between the worsening of the input conditions (groundwater level and PGA) and the increase of the liquefaction potential index in the test area.

The minimum and maximum scenarios are represented by IL_1 and IL_4 respectively, with areas going from low to extremely high LPI values. In addition, scenarios IL_2 and IL_3 show quite similar results with the same distribution of areas with high and extremely high LPIs. This demonstrated, in general, the same contribution of groundwater depth raises at ground level and the increase of PGA.

CPT values adopted for this study accounted for the results of single investigations. Interesting results on the uncertainties could also be provided by the analysis of the variability in the resistance parameters along profiles falling in the same cell or computation area.

A large source of uncertainty also deals with the input parameters adopted to characterize the soil resistance. In fact, it can be assessed through the use of three different in-situ investigation techniques, i.e., CPT, SPT, Vs. These methods carry on their own uncertainty in the assessment of mechanical parameters, as the latter are obtained from undirect approaches through empirical formulation. The perspective of the research could be the investigation of the variability of the results adopting different predisposing factors.

Finally, the assessment of the settlements induced by sand liquefaction will be evaluated. The above-mentioned sources of uncertainty could also provide some constrain on the variability of the expected settlement in the case study.

Liquefaction assessment methods, while essential for understanding seismic risk, are subject to various uncertainties. These arise from soil heterogeneity, empirical correlations, seismic loading variability, modelling assumptions, groundwater conditions, and potential errors in data collection. To mitigate these uncertainties, a combination of multiple assessment methods, site-specific studies, and probabilistic approaches are recommended. By understanding and addressing these uncertainties, it is possible to improve the reliability of liquefaction assessments and develop more robust designs for mitigating the risks associated with seismic-induced soil liquefaction.

7. Fourth Chapter: Applications of tools and toolchains for evaluating ground instabilities in marine (near-shore and coastal environments) contexts, with a focus on uncertainty quantification and sensitivity analysis

Edited by F. Zaniboni, S. Ceramicola, and A. Armigliato

7.1 Introduction

This document is a contribution to the deliverable "DV 2.4.8 - Scripting for uncertainty evaluation" (PNRR - PE3 RETURN), concerning the quantification of uncertainties in the use of the tools proposed in the previous phases of the project for the development of the Proof of Concept (PoC).

Here the purpose is to present the various conceptual steps undertaken by the "marine" research group to quantify the uncertainties associated with the tools and parameters used to explain the processes of detachment and sliding of a submarine landslide along an open slope located near the coastal area. The key steps involved are:

i) reconstruction of the failure dynamics of the three landslides identified along the slopes of the Ionian Calabrian Margin from marine high-resolution geophysical data;

ii) identification of the different geomorphological parameters of the three scenarios (perimeter, area, volume, position along the slope);

iii) quantification of the related tsunamigenic potential through numerical codes;

iv) assess the potential geohazard posed by the waves generated by the landslide scenarios;

v) assess the influence of the geomorphic parameters characterizing the three landslide scenarios on the tsunami generation through a sensitivity analysis and a parametric, empirical expression.

The overall purpose is to first obtain a quantification of the uncertainty, since the parametric expression allows one to quantify the effect of the landslide parameters on the respectively generated tsunami.

This report is organized as follows: the geological setting and constraints (7.2), with a description of the three landslide scenarios (7.2.1) and of the numerical methods (7.2.2) are introduced; the results of the simulations are then presented and discussed (7.2.3 and 7.2.4); the influence of landslide features on the tsunami generation is assessed through a sensitivity analysis (7.3), which offers a parametric expression that connects the geomorphic characteristics of the three landslides to the potentially resulting tsunami. This is compared to analogous formulas already available in the scientific literature. Finally, a discussion section (7.4) is presented, which includes specific considerations regarding uncertainty (7.4.1).

7.2 The Assi landslide complex

The Ionian Calabrian Margin (hereafter ICM), is part of the Tyrrhenian-Ionian subduction system and is a tectonically active margin shaped by mass movements of varying stiles, scales and ages (Ceramicola et al. 2024, Bianchini et al. 2024, Ceramicola et al. 2021, Ceramicola et al. 2014). The Punta Stilo Swell (see Figure 1) is a submerged lobate-shaped promontory within the Crotone-Spartivento area, closely tied to Calabria's kinematics (Mangano et al 2023), and is characterized by very steep slopes. The morphological data show that the continental margin here is characterized by a narrow continental shelf up to 10 km large, with maximum water depth reaching 1800 b.s.l., where most of the deposits resulting from collapses and erosion activity are placed.

The dynamics of the Assi multiple failures (see red box in Figure 7.1) have been reconstructed integrating high-resolution bathymetry with near-bottom seismic data and used to assess tsunamis hazard (Ceramicola et al., 2021; Ceramicola et al., 2014). Main geomorphic parameters of the three landslides, along with their

positions along the slope and the reconstructed failure dynamics, were used to assess the potential geohazards posed by the tsunamis that these events may have generated.

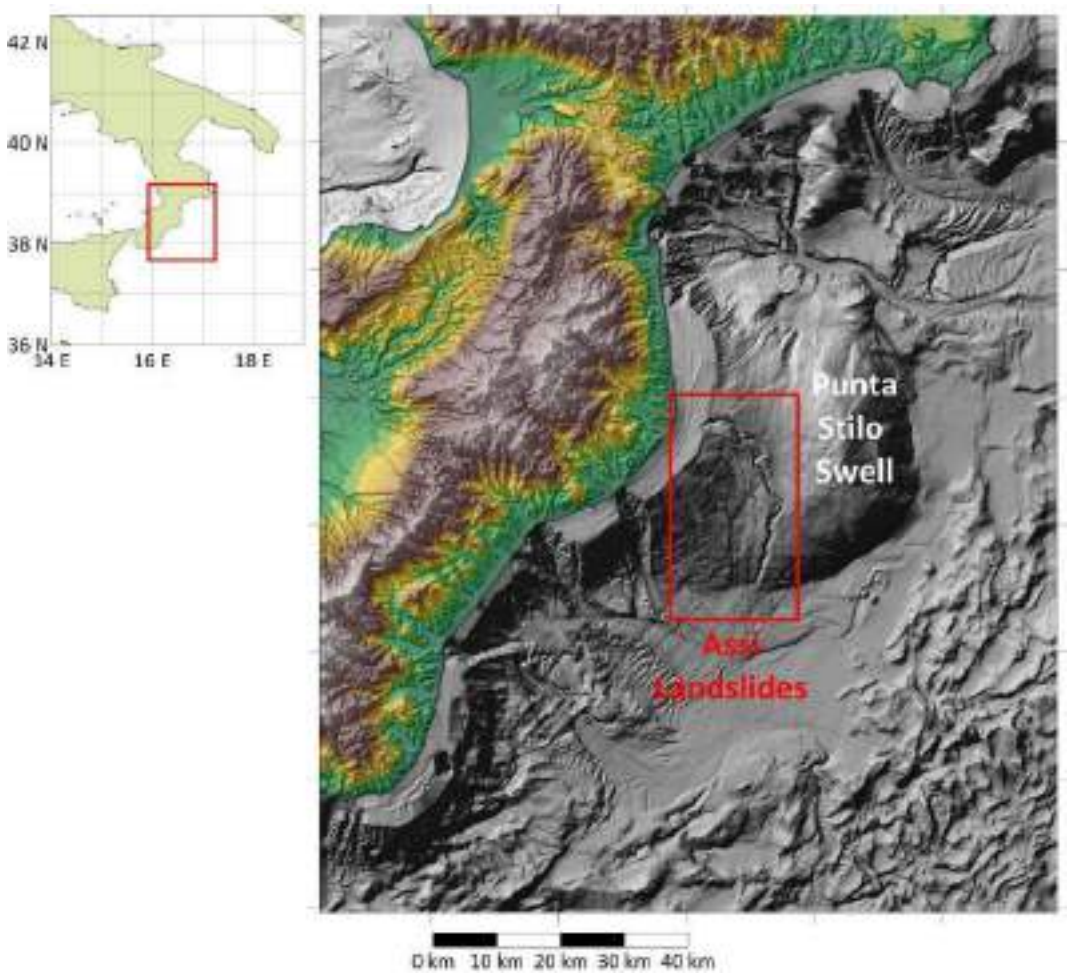

Figure 7-1. DTM of Ionian Calabrian Margin, South Italy. The red box marks the position of the Assi landslide complex, along the Punta Stilo Swell submarine slope.

7.2.1 Landslide scenarios

Three major interconnected landslides, varying in volume and size, occurred at water depths of approximately 200, 450, and 800 meters during the Holocene along the ICM: the oldest, about 4.3 kyrs BP, detached just below the shelf break (Slide 1, see Figure 7.2), only 8 km far from the Calabrian coast; the second and largest, involving the majority of the displaced material, happened at the base of the slope, around 2850 years ago; the third, likely triggered by the removal of material at its base (unbuttressing), occurred probably soon after the second higher up the ICM slope. These three events left distinct features from the failure, such as crowns, scarps, shear surfaces, and deposits, where sediment was displaced. Due to the sharpness of the scarps and the thickness of the overlying sediments, it was possible to tentatively reconstruct the age, shape, and volumes of the landslides (Ceramicola et al. 2024; Ceramicola et al., 2014).

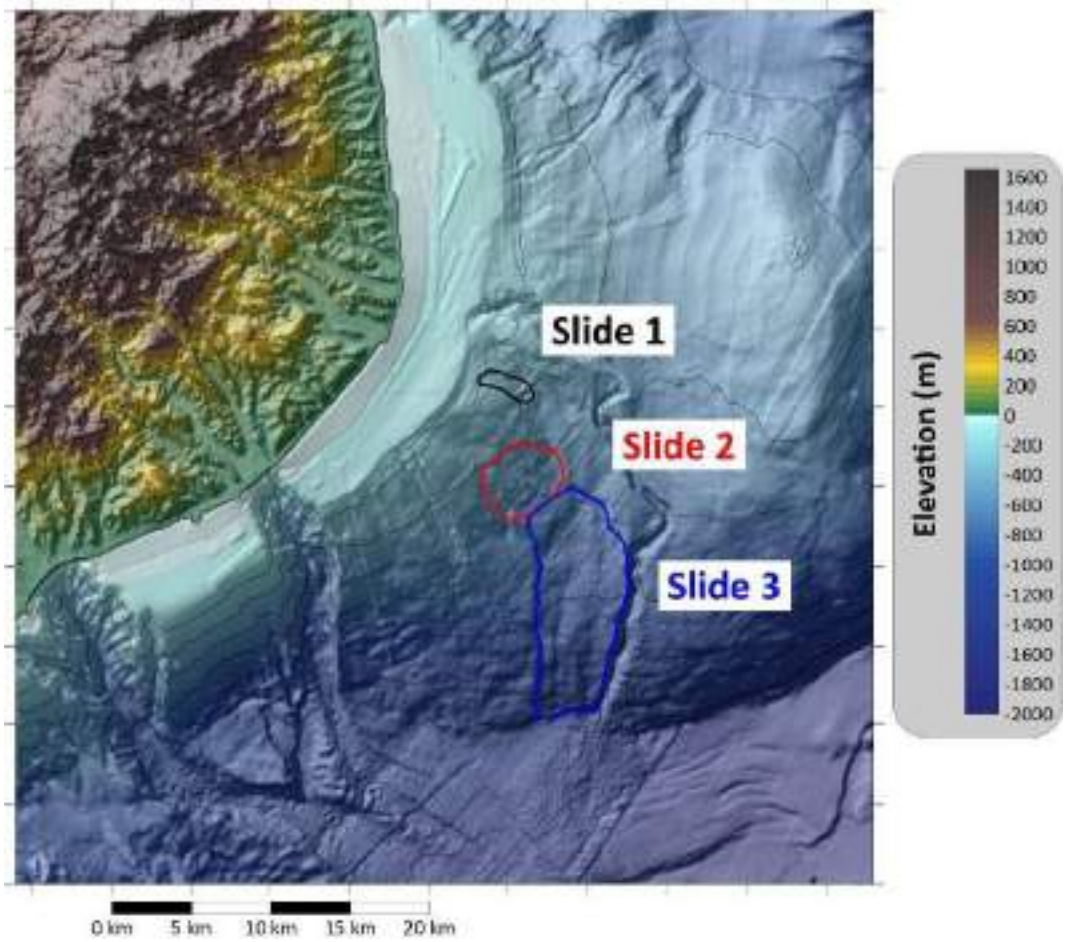

Figure 7-2. Map of the seabed with location of the three Assi submarine landslides: the black line indicates Slide 1, the oldest one, located only 8 km far from the Ionian Calabrian coast; in blue and red respectively Slide 3 and Slide 2, presumably occurring in sequence according to the reconstructed failure dynamics.

Based on the reconstructed failure dynamics and on the interpretation of morphological and seismic dataset, the main geomorphic parameters of the three landslide scenarios (areas and volumes), along with the detachment positions, have been reconstructed: the resulting landslides characteristics are reported in Table 7.1. It is worth to underline that the three events cover a wide range of possible collapses along submarine margins: a relatively small volume (around 50 million m3) at the top of the slope, close to the shelf (Slide 1); a huge mass (almost 2 km3) detaching in deep water, at the toe of margin (Slide 3); a landslide scenario detaching at intermediate depth with intermediate volume (Slide 2).

Notice also the low values for the mass thickness compared to areas involved in the collapse: this means that such scenarios can be considered shallow landslides, evolving soon into debris flow during the sliding motion, that are then characterized by large run-out. This feature is confirmed by the few deposits found along the margin (only for Slide 1 there is some evidence), while most of the material reaches the abyssal plain at its toe, at more than 1800 m depth. Such characteristic has an important role in the tsunami generation process and needs to be accounted for in the landslide dynamics simulation.

Table 7.1. Geomorphic characteristics of the three Assi landslides reconstructed through different sets of geophysical data (high-resolution bathymetry with near-bottom seismic data).

Slide	1	2	3
Min-Max Depth (m)	185 – 426	440 – 714	714 – 1422
Volume (km^3)	0.056	0.702	1.920
Area (km^2)	3.2	17.2	64.1
Maximum Thickness (m)	39.0	63.4	62.9
Mean Thickness	17.5	40.9	30.0

7.2.2 Overview on numerical techniques

The numerical techniques applied for the simulation of the Assi landslides and the consequent tsunamis have been developed and maintained in the years by Tsunami Research Team of the University of Bologna, and applied to many cases of landslide-tsunamis, both real (Scilla 1783, Zaniboni et al. 2016, Zaniboni et al, 2019; Stromboli 2002, Tinti et al., 2006) and potential (Marmara Sea, Gapserini et al., 2022; Gela Basin, Zaniboni et al., 2021; Marsili submarine volcano, Gallotti et al., 2021; Vavilov seamount, Gallotti et al., 2023).

The codes are applied in sequence, each one reflecting a specific phase of the phenomenon process. The landslide motion is simulated by means of the code UBO-BLOCK, described in detail in Tinti et al. (1997): in short, the sliding mass is partitioned into a set of interacting, volume-conserving portions, on the center of mass of which the motion equation is computed, taking into consideration all the forces acting on the mass, on its exposed surfaces and the mutual interactions among such portions. This allows the code to consider a crucial factor in terms of tsunamigenesis, i.e., the shape change of the mass during the descent, whose time history is one of the outputs provided. Table 7.2 lists the list of input required by the model and the output provided after its application.

The following phase considers the perturbation provided by the sliding motion on the sea bottom to the water column. Such impulse is not instantaneous, as for earthquake-tsunamis, but is time-dependent and represents the initial condition for the tsunami propagation. An intermediate code, named UBO-TSUIMP (described in Tinti et al., 2006), maps the seabed change due to landslide passage over the nodes of the tsunami computational grid, providing the water perturbation at each time step filtered through the sea depth. The deeper is the landslide, the smaller is the impulse provided. In Table 7.2 the list of input needed and the output resulting from this part of the numerical routine is reported.

The tsunami propagation is simulated through another numerical code, named UBO-TSUFD (for details, see Tinti and Tonini, 2013). This implements the shallow-water (SW) approach for the resolution of the hydrodynamic equations: such approximation is usually considered valid when the wavelength is much higher than the water depth where the perturbation propagates. For earthquake-generated tsunamis this condition is in general satisfied, while for landslide-tsunamis this depends on the source characteristics. Huge underwater masses are usually considered to fulfil this requirement, while for coastal, subaerial masses the dispersive effects become prevalent and cannot be neglected anymore. The SW equations are solved through a numerical scheme, implemented on a staggered grids configuration. Boundary conditions are of total transparency for open sea cells, while the interaction with the coast is regulated by the chosen approach: the shoreline can be considered as a vertical wall, imposing a minimum depth and not considering coastal flooding (linear version of SW equations); the sea-dryland limit can change, and flooding considered through the technique of moving boundary (non-linear version of the SW equations). As for the previous steps, in Table 7.2 input and output concerning this modelling are listed.

Table 7.2. List of input and output for the three codes accounting for the different phases of the landslide-tsunami process.

PHASE	INPUT	OUTPUT
Landslide dynamics	• Sliding surface (regular grid) • Upper surface of the sliding mass (regular grid) • Center of mass trajectory • Landslide lateral boundaries • Friction coefficient • Parameters accounting for landslide rheology	Landslide shape (blocks height, block length, basal area) and dynamics (acceleration, velocity, displacement, Froude number) time history
Tsunamigenic impulse	• Landslide shape and dynamics time history • Tsunami computational grid (bathymetry)	Dynamic tsunamigenic impulse on the nodes of the tsunami computational grids
Tsunami propagation	• Tsunamigenic impulse • Tsunami computational grid (bathymetry and topography) • Position of virtual tide gauges • Manning's coefficient (roughness)	• Tsunami propagation snapshots • Tsunami maximum amplitude on each node of the computational grid • Tsunami travel time on each node of the computational grid • Maximum water velocity on each node of the computational grid • Maximum flow depth on the nodes representing topography (in case of coastal flooding) • Synthetic marigrams, computed on the virtual tide gauges • Maximum Froude number, maximum momentum flux (in case of flooding)

7.2.3 Landslides: simulations results

The numerical routine described in the previous section is applied to the three Assi landslide events described in section 7.2.1. Figure 7.3 shows some output of the application of UBO-BLOCK to each case. In the first row, the central profile of the sliding motion is shown: the initial sliding masses are reported in blue, and the final simulated deposit in red. As mentioned in section 7.2.1, Slide 1 settles along the margin, between 700 and 800 m depth, while Slide 2 and Slide 3 reach the sub horizontal plateau at the ICM toe. In the first case the landslide run-out ranges 10-13 km, while for the other it reaches almost 30 km.

The lower row of plots portraits some information about the sliding dynamics, that is quite different for each case. Slide 1 is subjected to a strong acceleration (peak velocity of 17 m/s within 200 seconds), followed by a long deceleration phase. Slide 2 has a similar initial phase, reaching more than 20 m/s speed in 250 s, decelerates quickly and then accelerates again to 25 m/s, due to a steeper portion on the margin, at more than 1000 m depth. As to Slide 3, the acceleration is less abrupt than the other cases: the maximum value (around 17 m/s) is reached after more than 10 minutes, followed by a sudden deceleration.

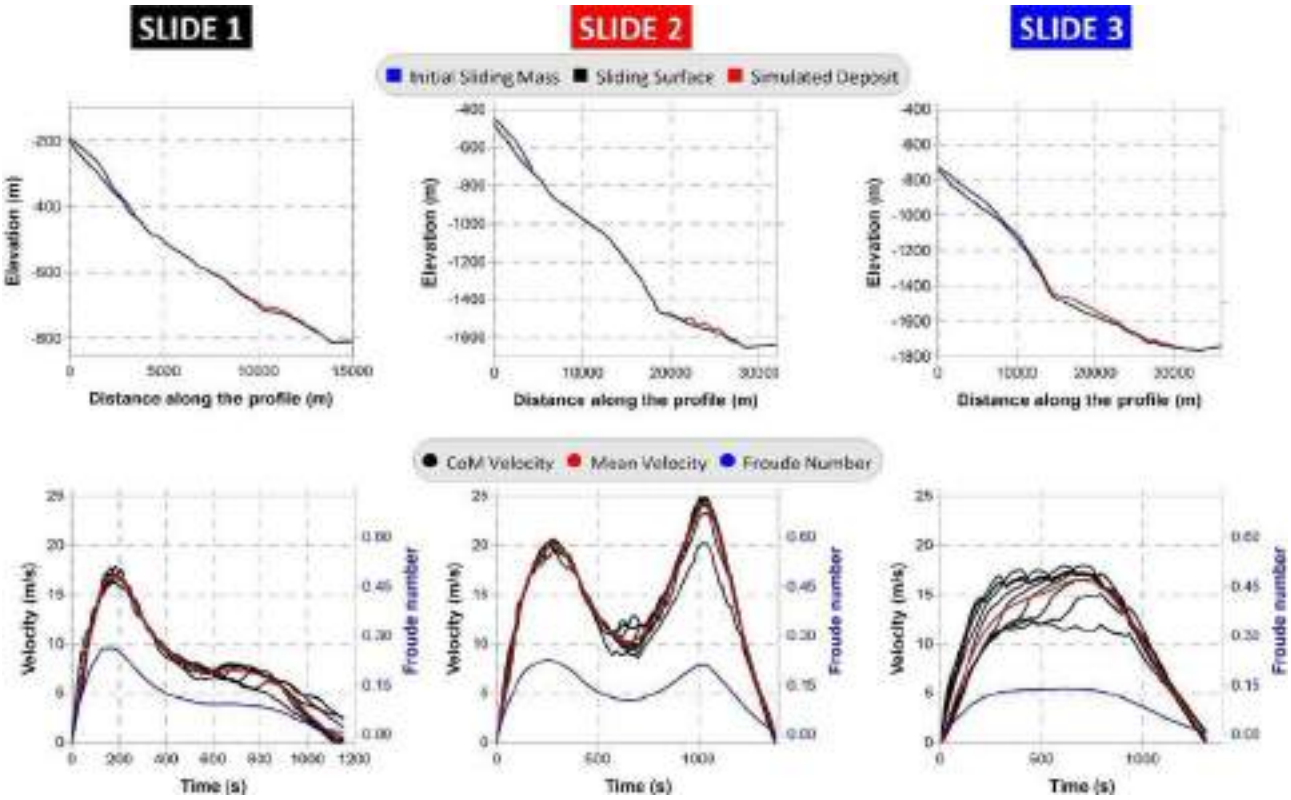

Figure 7-3. UPPER ROW: Profiles along the sliding surface for the three Assi landslides: in blue the initial mass, in red the final simulated deposit, in black the undisturbed sliding surface. LOWER ROW: Sliding dynamics for the three Assi failure scenarios: in bl ack the velocity of the blocks centre of mass, in red the average velocity and in blue the Froude number temporal evolution.

The blue lines mark the Froude number (Fr) time history: this is computed as the ratio between the velocities of the wave (depending, in the SW approximation, only on the water depth) and of the landslide. When the two values are close (then $Fr = 1$), the energy transfer from the mass to the wave is at the maximum efficiency. Lower or larger values correspond to subcritical or supercritical regimes, where the wave and the landslide move at different velocities and the interaction is smaller. For the scenarios here studied, Fr shows always subcritical values, reaching a maximum of 0.3 for Slide 1 in its acceleration phase. Notice that the values are lower for increasing depth: in Slide 2, for example, the second velocity peak, higher than the first, corresponds to a smaller peak for Fr, since this happens in deeper water, where the wave velocity is bigger.

7.2.4 Tsunamis: simulation results

As mentioned in paragraph 7.2.3, the sliding motion provides the input for the tsunami generation. Among the many outputs of the code UBO-TSUFD, here some of most interesting are reported and described in brief. At first, Figure 7.4 shows the maximum tsunami amplitude over each node of the computational grid (that has been realized with a spatial resolution of 100 m). This kind of plot is very useful, since it provides a glance of the wave energy distribution in the studied domain, allowing the identification of the coastal stretches more affected by the tsunami impact.

It can be noticed that the scenario providing the most impacting waves is Slide 2, with maximum amplitudes reaching 2 m from Roccella Jonica (point#2 in the map) to Soverato (#4). Slide 3, the most voluminous and

deep, generates lower effects on the coast; Slide 1, although closest to the shoreline and shallowest, generates significantly smaller waves compared to the other two scenarios.

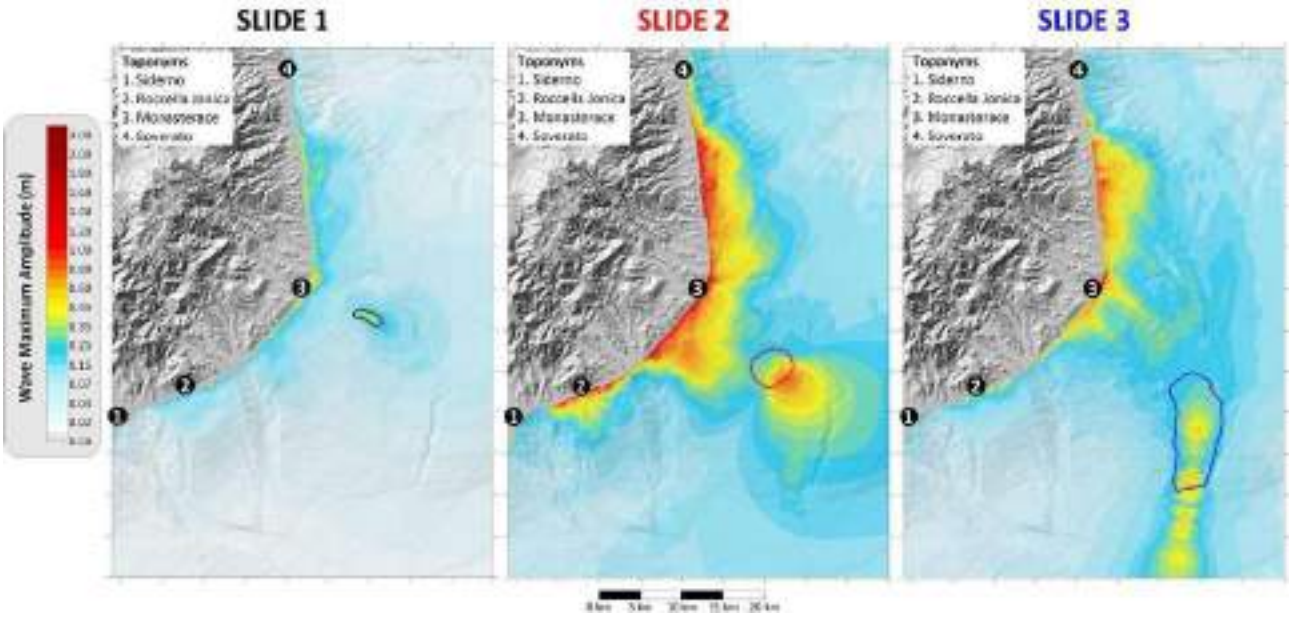

Figure 7-4. Maximum tsunami amplitude over each node of the computational grid for the three Assi failures events. The colour association to the amplitude of the wave is shown in the colour bar on the left: red corresponds to the higher values. The numbered black circles mark the position of some toponyms along the coast. The coloured boundaries (black, red and blue) show the initial position of the tsunamigenic landslide for each scenario.

A comparably effective view of the tsunami impact on the shoreline can be seen in Figure 7.5: here the maximum tsunami amplitude is plotted against the cumulative distance along the coast, whose origin is placed here on the northern extreme of the computational grid. The graph confirms the previous observations about the tsunami generation: along the entire extension of the coast (in the computational domain) the most extreme amplitudes (positive and negative) are associated to Slide 2, with peaks of more than 1.5 m at Monasterace (#3) and half-way between Monasterace and Soverato (#4), in the correspondence of the largest shelf extension. Lower values are attained for Slide 3 (slightly less than 1.5, again Monasterace), while Slide 1 generates smaller waves, ranging half meter maximum.

An interesting feature can be deduced by the observation of the maximum amplitude decay from point #3 towards #1: this is approximately linear with distance, apart from two sudden "depressions" in correspondence with cumulative coastal distances of 45 km and 60 km (right plot, Figure 7.5). The map on the left shows that such values coincide with two submarine canyons whose head is almost on the shoreline: due to their presence, the water close to the coast is deeper, and the waves reaching the coast are then faster and lower.

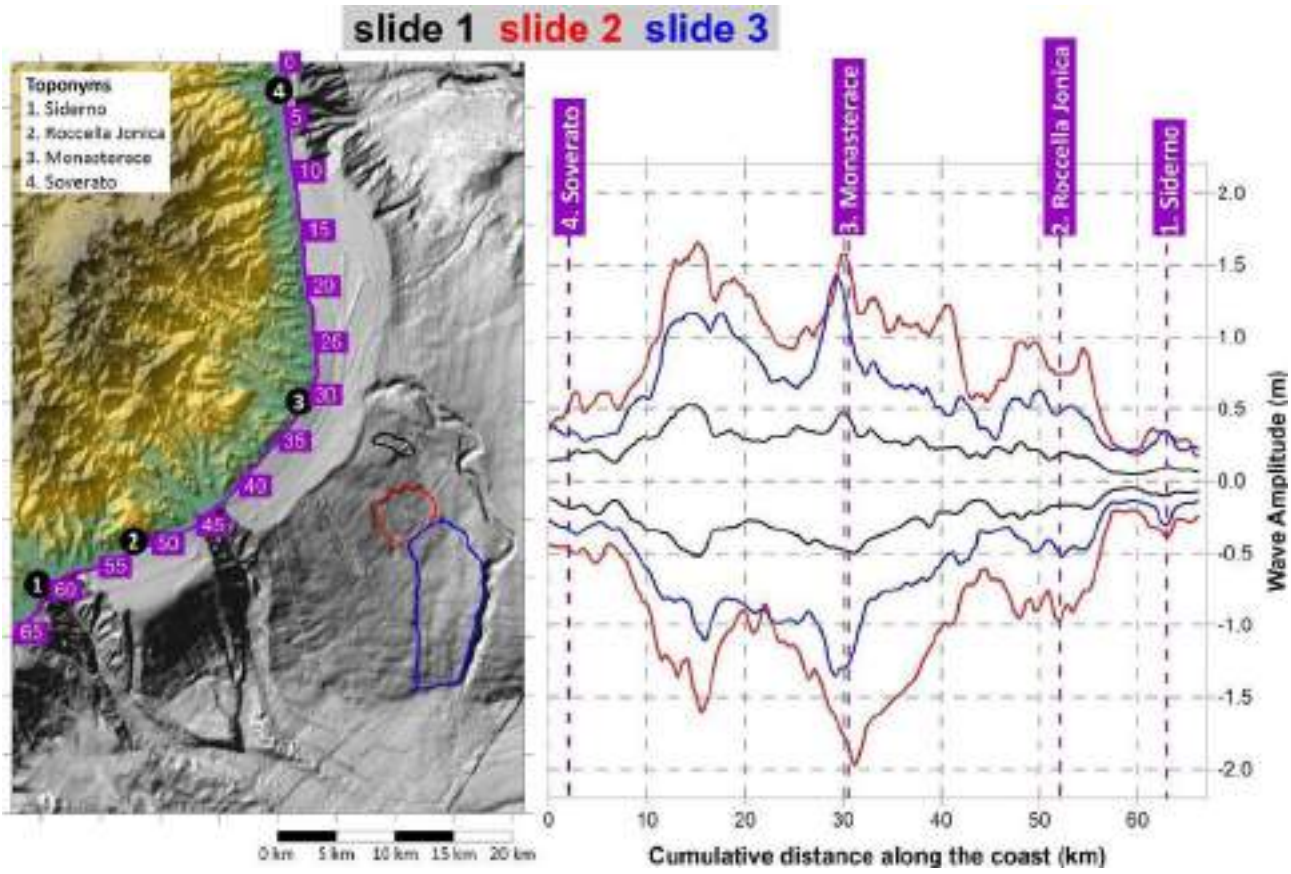

Figure 7-5. LEFT PLOT) DTM of the Ionian Calabrian Margin with position of the reconstructed boundaries of the Assi landslides (black, red and blue), showing the cumulative distance along the coast starting from the northern extreme. Black dots indicate toponyms. RIGHT PLOT) Maximum water amplitude at the shoreline, plotted against the cumulative distance along the coast. Purple dotted lines mark the positions of the coastal toponyms.

7.3 Sensitivity Analysis

The results reported in the previous section show that the tsunami amplitude at the coast does not depend simply on the landslide size: the larger mass (Slide 3) generates waves lower than Slide 2, that is less voluminous. Similar considerations can be done for other geomorphic parameters such as the landslide detachment depth, since the shallower case (Slide 1) produces smaller waves compared to the other scenarios, occurring in deeper water.

It is worthwhile then trying to assess the influence of some parameters describing the landslide on the ensuing tsunamis through a sensitivity analysis. The investigation moves from the already simulated cases, building new "derived" scenarios by simply multiplying the initial mass thickness by a factor α: Table 7.3 shows the values of such factor, ranging the interval $[0.25 - 2]$, providing then new masses with volumes from a quarter to twice the starting scenarios (shown in the fourth column). The numerical routine, previously applied to the three original scenarios, is then run for the new additional landslides, that are six for each case. A total of 21 landslide and tsunami simulations are then obtained: the last column of Table 7.3 reports the maximum tsunami amplitude along the coast attained by these new applications of the numerical code.

Table 7.3. List of the "derived" scenarios obtained from the three original ones (in grey), with some parameters characterizing the sliding mass (initial thickness and volume) and the resulting tsunami (maximum amplitude on the coast). α: multiplying factor; H_{max}: maximum landslide initial thickness; V: landslide volume; η_{max}: maximum tsunami amplitude on the coast.

case	α	H_{max} (m)	V (km^3)	η_{max} (m)
1A	0.25	9.8	0.014	0.12
1B	0.5	19.5	0.028	0.23
1C	0.75	29.3	0.042	0.35
1	1	39.0	0.056	0.58
1D	1.25	48.8	0.070	0.62
1E	1.5	58.5	0.084	0.76
1F	2	78.0	0.113	1.03
2A	0.25	15.9	0.176	0.44
2B	0.5	31.7	0.351	0.85
2C	0.75	47.6	0.527	1.31
2	1	63.4	0.702	1.80
2D	1.25	79.3	0.878	2.32
2E	1.5	95.1	1.053	2.83
2F	2	126.9	1.404	3.83
3A	0.25	15.7	0.480	0.25
3B	0.5	31.4	0.960	0.55
3C	0.75	47.2	1.440	0.97
3	1	62.9	1.920	1.57
3D	1.25	78.6	2.400	1.92
3E	1.5	94.3	2.880	2.30
3F	2	125.8	3.840	3.11

The results obtained in Table 7.3 suggest that, for each group of scenarios, for which some parameters are almost the same (detachment depth, area, slope, distance from the coast, etc.), the volume and the maximum tsunami amplitude on the coast (η_{max}) seem to be correlated: when the first is halved (scenarios B), the second changes accordingly; when the volume is doubled (scenarios F), the same happens to the tsunami amplitude, within an acceptable range.

The data from Table 7.3 are shown in Figure 7.6 using a log-log plot: within each group of scenarios, the different cases are fairly well aligned. The computation of the linear fits (represented by the dashed lines) indicates that they have nearly identical slopes, with values close to 1 (see Table 7.4). This confirms a linear correlation between the tsunami amplitude at the coast and the landslide volume. The difference among the three lines (and thus among the three groups of scenarios) stands in the y-axis intercept, meaning that probably other parameters characterizing the landslide influence the tsunami generation and should be accounted for.

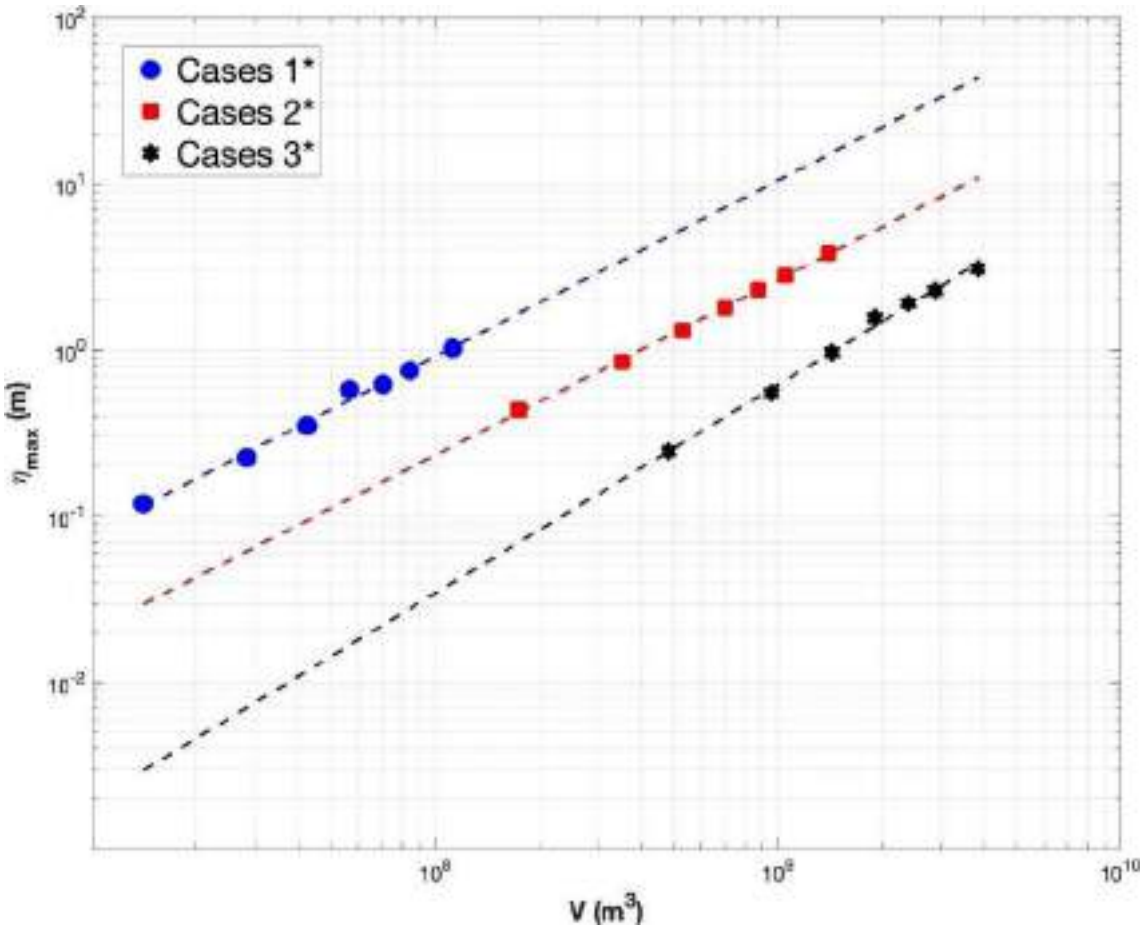

Figure 7-6. Log-log plot of the tsunami amplitudes vs the respective landslide volume for the original and "derived" Assi landslides scenarios: in blue cases from 1A to 1F, in red 2A-2F, in black 3A-3F (see Table 7.2). The dashed lines mark the respective linear fit.

Table 7.4. Parameters of the linear fits for each group of landslide-tsunami scenario (see Figure 7.6)

$\eta_{MAX} = AV + B$			
Scenario	A	B	R^2
1*	1.06	-8.49	0.991
2*	1.05	-9.06	0.999
3*	1.25	-11.49	0.995

To evaluate the impact of the various geomorphic parameters used to reconstruct the failure events and their potential for tsunami generation, additional factors must be considered. This can be achieved by examining combinations of landslide geomorphic parameters and evaluating their correlation with the outcomes of the tsunami simulations. Regarding the first factor, the phenomenon can be described and parameterized through various elements that characterize the mass's geometry, its rheology, and the sliding dynamics. As the focus here is on the tsunamigenic process, the selection specifically emphasizes the following factors:

- the landslide initial sea-depth (D)
- the average slope gradient of the rupture surface (θ)
- the landslide volume (V)

- the minimum distance of the landslide crown from the coast (d)
- The metric adopted for the evaluation of the ensuing tsunami is:
- the maximum wave amplitude on the coast (η_{SIM}), retrieved through the numerical simulations

The combination of the landslide parameters is realized by elevating each quantity to its own exponent, which ranges a predefined interval spanned through a regular step. A new quantity is obtained as the product of these power laws, whose correlation with η_{SIM} is then measured by means of the correlation parameter R^2. The set of exponents providing the highest value of R^2 is then chosen as the most suitable one. The described procedure produced the following expression:

$$\eta_{NEW} = 0.262 \frac{V^1 (sin\theta)^{1.7}}{D^{1.1} d^{0.7}} - 0.0524 \quad (1)$$

with a correlation value $R^2 = 0.997$. The parametric expression (1) for η_{NEW} confirms the linear correlation between the tsunami amplitude and the volume and provides also an esteem of the effect of the other parameters: the slope gradient θ is the quantity with the highest exponent (thus the most influent), underlining the importance of the initial inclination of the landslide, affecting the initial acceleration of the mass and consequently the wave generation. Moreover, it is not surprising to get negative exponents (meaning anti-correlation) for the slide sea-depth and its distance from the coast: both quantities, when growing, produces lowering of the tsunami at the coast, with slight predominance of D with respect to d.

Parametric laws as the one expressed by (1) are frequent in the scientific literature, especially when dealing with complex phenomena affected by highly non-linear processes, as it's the case for landslide-tsunamis. Such expressions are obtained typically with an empirical approach and are based mainly on simulations (since no extensive and comprehensive catalogues of landslide-tsunami effects exist) and link the tsunami amplitude to some landslide characteristics. The first here presented as a term of comparison comes from Rahiman and Pettinga (2006):

$$\lambda = 3.87 \cdot \left(\frac{bD}{sin\theta}\right)^{0.5} \quad (2a)$$

$$\eta_{RB} = 0.224 \cdot T\left[\frac{w}{w+\lambda}\right] \cdot [(sin\theta)^{1.29} - 0.746 \cdot (sin\theta)^{2.29} + 0.170 \cdot (sin\theta)^{3.29}] \left(\frac{b}{D}\right)^{1.25} \quad (2b)$$

With: λ, tsunami wavelength; b, initial length of failure mass perpendicular to the margin; D, initial water depth at the middle of failure mass; θ, mean slope of failure scar; T, maximum initial failure mass thickness normal to slope; w, initial width of failure mass parallel to margin. The result, η_{RP}, is the tsunami amplitude at the coast obtained adopting this approach.

Another similar expression can be retrieved from Zengaffinen-Morris et al. (2022), who considered the submarine landslides database of the Gulf of Cadiz (Spain, Atlantic Ocean) and the respective simulated tsunamis. The equation is:

$$\eta_{ZM} = 0.073 \cdot \left[\frac{(sin\theta)^2 V}{D^2 F^{0.3}}\right]^{0.89} \quad (3)$$

With: θ, mean slope of failure scar; V, volume; D, initial water depth at the middle of failure mass; F, safety factor, accounting for slide instability. The obtained value is the tsunami amplitude close to the coast, which is here denoted with η_{ZM}. Both approaches confirm that the greatest control on the tsunami features is given by the slope parameters $sin\theta$ and D, with similar values for the respective exponents; equation (3) confirms also the almost linear dependance of the tsunami amplitude from the volume V of the landslide.

When using the geomorphic parameters of the 21 Assi scenarios into equations (1), (2) and (3), an esteem of the expected tsunami amplitudes based on such expressions is obtained. Figure 7.7 reports the comparison among the values obtained from the simulations (black triangles) and the ones through the expression here introduced (blue circles, marked with NEW) and the two from literature (green and red for RP and ZM respectively). It is clear that the last two approaches lead to an underestimation of the generated wave, which is accurately reconstructed by the values obtained through expression (1), developed using this data.

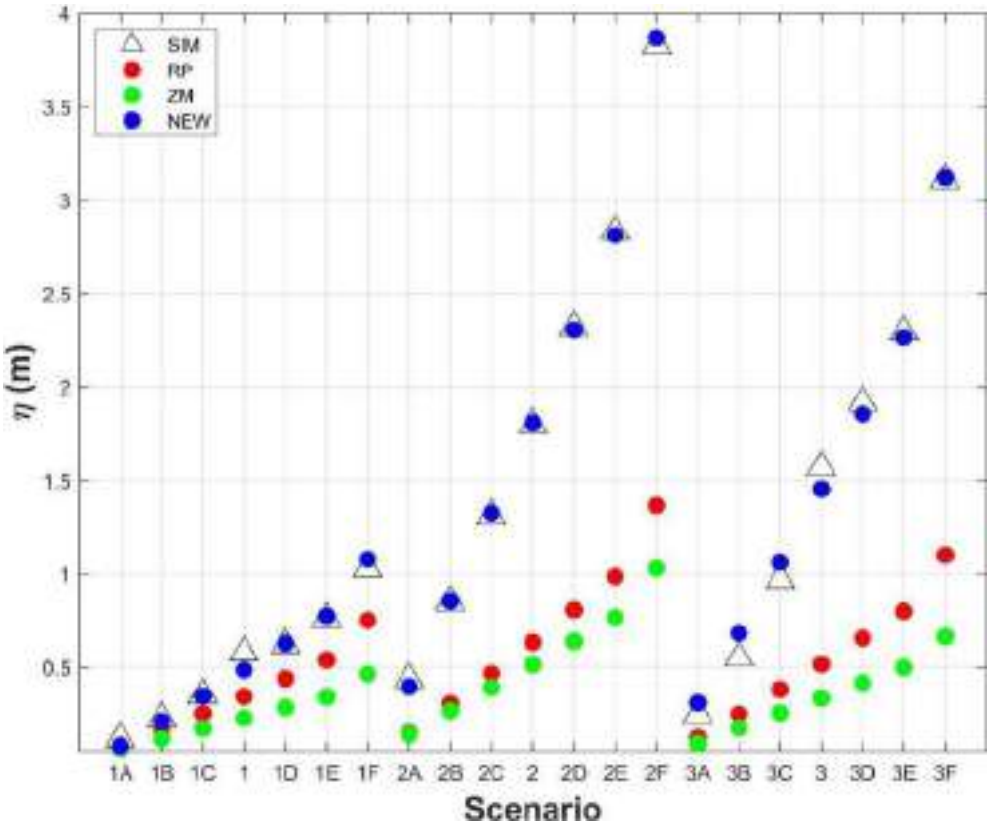

Figure 7-7. Maximum tsunami amplitude for the Assi landslide scenarios obtained from equations (1), (2) and (3), marked respectively with the blue, red and green circles. Black triangles report the values obtained from the numerical simulations.

7.4 Discussion and Conclusions

Three landslide events have been identified and reconstructed integrating high-resolution bathymetry with near-bottom seismic data. Their failure dynamics have been used to assess tsunamis hazard along a stretch of the Ionian Calabrian coast. Numerical simulations indicate that neither the larger mass nor the shallower one generates the highest tsunami amplitude along the coast.

This observation prompted a sensitivity analysis aiming at exploring the impact of the geomorphic parameters of the landslides on the tsunami generation. Moving from the three reconstructed failure events, the respective initial thickness have been multiplied by a set of factors, adding new cases, with different volumes, for a total of 21. A connection has been recognized between the volume of sediment evacuated and the tsunami amplitude, showing a linear correlation between the two quantities. However, it is also evident that other parameters play a relevant role in the landslide-tsunami interaction.

Further investigation involved also other landslide features that characterize the three Assi landslides, such as detachment sea-depth, slope gradient and distance from the coast. This led to the definition of a new parametric expression that relates these values to the tsunami amplitude along the coast, which was then compared to other empirical formulas found in the literature. It was found that the initial detachment slope gradient exerts the highest control on tsunami generation. Additionally, both volume and detachment sea-depth play relevant roles, while distance from the coast should not be disregarded.

These results are affected by many limitations, that can be grouped and listed as follow:

i) these results were been obtained in a specific area, the Ionian Calabrian Margin, and they should be considered valid only for similar morphologies and geological conditions, rather than being broadly applicable;
ii) the scenarios adopted to obtain the parametric expression use a variation of the three initial events: the variation of detachment sea-depth and distance from the coast do not encompass a wide range of values and should be expanded to include a larger database of events;
iii) the entire approach relies on numerical simulations, owing to the limited availability of submarine landslides cases studied. Additionally, reconstructing reliable geomorphic parameters and failure dynamic is complex, involving acquisition of costly underwater geophysical and geological data;
iv) the use of modelling introduces many uncertainties, that are very difficult to quantify and will be in part discussed in the following section (7.4.1), but is often the only way to assess the tsunami hazard along a coastal stretch. The parameter expression here obtained provides an approximate quantification of the expected tsunami, as it does not account for non-linear coastal effects and local bathymetric features (such as shoaling, edge waves, basin resonance, reflection) which can significantly influence the tsunami's impact on the coast.

For all these reasons, the results presented here should not be considered universally valid; rather, they can offer valuable insights for more detailed investigations in the submarine environment, assisting in directing research (and economic) effort toward specific events or areas. The significance of the obtained result indicates that, within 3 to 5 minutes, waves exceeding 1 m amplitude can impact the southern Calabrian coast, with the potential to damage coastal infrastructures and to be amplified in small harbors. This proves that tsunamis represent a hazard for Ionian coastal areas, and call for accurate monitoring and further study.

7.4.1 Considerations about uncertainty

The quantification of the uncertainty in the numerical simulation of natural events is usually very complex, due to the many factors entering its assessment. For this brief discussion, the reference is the structure reported in "DV 2.4.7 - Checklist to identify the contexts and geohazard indicators subjected to uncertainty", with three phases characterizing the workflow for the evaluation of the uncertainty that will be discusses separately in the following: 1) Investigating the uncertainty in input data; 2) Sensitivity analysis; 3) Modelling framework to deal with uncertainties.

- **Investigating the uncertainty in input data**

This issue covers different phases of the study, from data gathering and set-up to the numerical simulation requirements:

i) In marine realm, uncertainty usually relates to the techniques, and thus acoustic parameters, used to acquire the geophysical dataset. Both when using information derived by swath bathymetry and acoustic sub-bottom profiling data, the uncertainty can be linked to several factors including data resolution. Spatial resolution affects the level of detail that can be captured. Higher resolution provides finer details but may introduce more noise, while lower resolution reduces detail,

potentially missing critical features. Vertical and horizontal resolution affect the ability to distinguish small depth changes and fine features in sub-bottom layers. Coarser resolution can lead to an underrepresentation of complex topography or stratigraphy. However, when using acoustic data, we should take in account instrumental factors (beam angle and coverage, frequency of acoustic waves and sound speed variability) as well as environmental factors such as water column conditions, seabed composition. The resolution of data is a key component of uncertainty, but it interacts with many other factors that all contribute to the overall quality and reliability of the dataset. In the specific of the tool here presented, the input data used for the numerical modelling are reported in Table 7.2, and are mainly extracted from seabed bathymetry and on land topography: uncertainty, especially for the second, is usually very low, compared to the other assumptions that are made during the whole process.

ii) The initial landslide volume reconstruction is estimated using morphological considerations that can introduce large degree of uncertainty, of difficult quantification; similarly for the other quantities related to the landslide simulation input.

iii) Concerning the parameters accounting for the landslide dynamics, the friction coefficient is usually adjusted to fit the observed landslide deposit and the landslide run-out (when available); the parameters governing the slide deformation are set to reproduce the expected rheology of the slide. In these specific cases, for landslide 1 (Figure 7.2) the evacuated sediment (landslide deposit) is observed to lie along the margin, where successively landslide 2 and 3 will indent the seabed, while the deposits of landslides 2 and 3 are observed to reach the toe of the margin in deeper water: the parameters have been then set up in order to fit such pieces of evidence, i.e., translational landslides with large run-out and consistent deformation.

iv) The computational grid realization itself introduces some approximation, since the codes need a regularly spaced grid that is realized through interpolation of the raw data. Connected to this, apart from these interpolation effects, the data describing the interface water-dryland need readjustment to avoid numerical instabilities, meaning that the "real" coastline can be slightly different from the "computational" one.

For each of such topics the single quantification of the uncertainty is difficult; furthermore, each factor can impact the final assessment at very different scale, enhancing considerably the degree of arbitrariness in this evaluation.

- **Sensitivity analysis**

In this phase the uncertainty introduced by modelling is considered, then the influence that all the parameters and the quantities used have on the result produced. The investigation presented here have been carried out mainly in this direction, presenting an estimation of the landslide parameters control on the tsunamigenesis.

- **Modelling framework to deal with uncertainties**

In the final step of the procedure, a probabilistic framework should be applied to account for the uncertainty propagation along the different phases of the hazard assessment process. This kind of investigation is becoming the standard for tsunamis generated by earthquakes, adopting an approach that is similar to the seismic hazard assessment (see for a review Behrens et al., 2021). For tsunamis generated by landslides the procedure is less developed, due also to the different characteristics of the phenomenon itself. A preliminary approach, addressing both landslide-tsunamis as well as earthquake-tsunamis, is presented in the work by Grezio et al. (2012). In this study, the authors have developed a procedure to estimate the probability of exceeding a tsunami run-up of 0.5 meters in one year for the area of the Straits of Messina.

8. References

Anderson, D., Franke, K.W., Dashti, S., Badanagki, M., Kayen, R., 2019. The over-prediction of liquefaction in alluvially deposited volcanic sediments, Earthquake Geotechnical Engineering for Protection and Development of Environment and Constructions. CRC Press, pp. 1122-1129.

Behrens J., Løvholt F., Jalayer F., Lorito S., Salgado-Gálvez M.A., Sørensen M., Abadie S., Aguirre-Ayerbe I., Aniel-Quiroga I., Babeyko A., Baiguera M., Basili R., Belliazzi S., Grezio A., Johnson K., Murphy S., Paris R., Rafliana I., De Risi R., Rossetto T., Selva J., Taroni M., Del Zoppo M., Armigliato A., Bureˇs V., Cech P., Cecioni C., Christodoulides P., Davies G., Dias F., Bayraktar H.B., González M., Gritsevich M., Guillas S., Harbitz C.B., Kanoglu U., Macías J., Papadopoulos G.A., Polet J., Romano F., Salamon A., Scala A., Stepinac M., Tappin D.R., Thio H.K., Tonini R., Triantafyllou I., Ulrich T., Varini E., Volpe M., Vyhmeister E. (2021). Probabilistic Tsunami Hazard and Risk Analysis: A Review of Research Gaps. Front. Earth Sci., 9, 628772, doi: 10.3389/feart.2021.628772.

Beven K. J., R. Lamb, P. Quinn, R. Romanowicz, and J. Freer, 1995. TOPMODEL, in V.P. Singh (Ed.). Computer Models of Watershed Hydrology. Water Resources Publications

Bianchini M., Ceramicola S., Casalbore D., Chiocci F.L. (2024), Analysing submarine landslide distribution along the Calabrian continental margins, insights from high-resolution morpho-bathymetric data. The 37th International Geological Congress 2024. August 25-31, 2024, Busan, Republic of Korea.

Boulanger, R.W., Idriss, I.M., 2014. CPT and SPT based liquefaction triggering procedures. Report No. UCD/CGM.-14, 1, 134.

Ceramicola S., Cova A., Forlin E., Markezic N., Mangano G., F. Civile, M., M. Zecchin, F. Fanucci, E. Colizza, C. Corselli, D. Morelli, A. Savini, A. Caburlotto, O. Candoni, M. Coste, D. Cotterle, S. Critelli, A. Cuppari, M. Deponte, R. Dominici, L. Facchin, E. Gordini, M. Locatelli, F. Muto, D. Praeg, R. Romeo, C. Tessarolo, (2024). Geohazard features of the Ionian Calabrian Margin. (20), 1.

Ceramicola S., Fanucci, F., Corselli, C., Colizza, E., Morelli, D., Cova, A. Savini, A., Praeg, D., Zecchin, M., Caburlotto, A., Candoni, O., Civile, D., Coste, M., Cotterle, D., Critelli, S., Cuppari, A., Deponte, M., Dominici, R., Forlin, E., Gordini, E., Tessarolo, C., Marchese, F., Muto, F., Palamara, S., Ramella, R., Facchin, L., & Romeo R. (2021). Tavola 8.Calabria Ionica, pag. 174-192 in: F.L.Chiocci et al (2021) Atlante dei lineamenti di pericolosità geologica dei mari italiani- Risultati del progetto. CNR edizioni, Roma.

Ceramicola S., Tinti S., Zaniboni F., Praeg D., Planinsek P., Pagnoni G., Forlin E. (2014), Reconstruction and tsunami modeling of a submarine landslide on the Ionian margin of Calabria (Mediterranean Sea), K. Sassa, P. Canuti, Y. Yin (eds.), Landslide Science for a Safer Geoenvironment, Vol. 3, pp. 557-562, doi: 10.1007/978-3-319-04996-0_85, © Springer International Publishing Switzerland 2014.

Chiaradonna, A. et al., 2018. Numerical simulation of soil liquefaction during the 20 May 2012 M6. 1 Emilia Earthquake in Northern Italy: the case study of Pieve di Cento, pp. 18-21.

Cubrinovski, M., Rhodes, A., Ntritsos, N., Van Ballegooy, S., 2019. System response of liquefiable deposits. Soil Dynamics and Earthquake Engineering, 124, 212-229.

Gallotti G., Zaniboni F., Arcangeli D., Angeli C., Armigliato A., Cocchi L., Muccini F., Zanetti M., Tinti S., Ventura G. (2023). The tsunamigenic potential of landslide-generated tsunamis on the Vavilov seamount. Journal of Volcanology and Geothermal Research, 434, 107745. https://doi.org/10.1016/j.jvolgeores.2023.107745.

Gallotti G., Zaniboni F., Pagnoni G., Romagnoli C., Gamberi F., Marani M., Tinti S. (2021), Tsunamis from prospected mass failure on the Marsili submarine volcano flanks and hints for tsunami hazard evaluation. Bulletin of Volcanology (2021) 83: 2. https://doi.org/10.1007/s00445-020-01425-0.

Gasperini L., Zaniboni F., Armigliato A., Tinti S., Pagnoni G., Özeren M. S., Ligi M., Natali F., Polonia A. (2022), Tsunami potential source in the eastern Sea of Marmara (NW Turkey), along the North Anatolian Fault system. Landslides, 19:2295–2310. DOI 10.1007/s10346-022-01929-0.

Grezio A., Sandri L., Marzocchi W., Argnani A., Gasparini P., Selva J. (2012). Probabilistic tsunami hazard assessment for Messina Strait area (Sicily, Italy). Nat. Hazards, 64, 329-358, doi: 10.1007/s11069-012-0246-x.

Mangano G., Zecchin M., Civile D., Ceramicola S., Donato A., Muto F., ... Critelli, S. (2022). Mid-Miocene to recent tectonic evolution of the Punta Stilo Swell (Calabrian arc, southern Italy): an effect of Calabrian arc migration. Marine Geology, 448, 106810. https://doi.org/10.1016/j.margeo.2022.106810

NTC, 2018. Norme Tecniche per le Costruzioni, CS.LL.PP. Gazzetta Ufficiale della Repubblica Italiana, n. 42, 20 febbraio, Suppl. Ordinario n. 8. Ist. Polig. Rome e Zecca dello Stato S.p.a.; 2018. (in Italian)

Idriss, I.M., Boulanger, R.W., 2006. Semi-empirical procedures for evaluating liquefaction potential during earthquakes. Soil dynamics and earthquake engineering, 26, 115-130.

Idriss, I.M., Boulanger, R.W., 2008. Soil liquefaction during earthquakes. Earthquake Engineering Research Institute. Oakland, CA.

Ishihara, K., Yoshimine, M., 1992. Evaluation of settlements in sand deposits following liquefaction during earthquakes. Soils and foundations, 32, 173-188.

Iwasaki, T., Arakawa, T., Tokida, K.-I., 1984. Simplified procedures for assessing soil liquefaction during earthquakes. International Journal of Soil Dynamics and Earthquake Engineering, 3, 49-58.

Lai, C.G., Bozzoni, F., Mangriotis, M.-D., Martinelli, M., 2015. Soil liquefaction during the 20 may 2012 M5. 9 Emilia earthquake, northern Italy: Field reconnaissance and post-event assessment. Earthquake Spectra, 31, 2351-2373.

Liao, S.S.C., Whitman, R.V., 1986. Overburden correction factors for SPT in sand. Journal of geotechnical engineering, 112, 373-377.

NTC, 2008. Norme tecniche per le costruzioni. Decree of the Minister of the Infrastructures, 14.

Robertson, P.K., 1991. Soil classification using the cone penetration test: Reply. Canadian geotechnical journal, 28, 176-178.

Rahiman T. I. and Pettinga J. R. (2006). The offshore morpho-structure and tsunami sources of the Viti Levu Seismic Zone, southeast Viti Levu, Fiji. Marine Geology, 232(3-4), 203-225. https://doi.org/10.1016/j.margeo.2006.07.007.

Robertson, P.K., Campanella, R.G., 1985. Liquefaction potential of sands using the CPT. Journal of geotechnical engineering, 111, 384-403.

Rollo F., Rampello S., 2023. Evaluation of Seismic Landslide Hazard Based on a New Displacement Semi-empirical Relationship. In: Ferrari, A., Rosone, M., Ziccarelli, M., Gottardi, G. (eds) Geotechnical Engineering in the Digital and Technological Innovation Era. CNRIG 2023. Springer Series in Geomechanics and Geoengineering. Springer, Cham. https://doi.org/10.1007/978-3-031-34761-0_74

Seed, H.B., Idriss, I.M., 1971. Simplified procedure for evaluating soil liquefaction potential. Journal of the Soil Mechanics and Foundations division, 97, 1249-1273.

Silvestri, F., D'Onofrio, A., 2014. Risposta sismica e stabilità di centri abitati e infrastrutture, La Geotecnica nella difesa del territorio e delle infrastrutture dalle calamità naturali. AGI, pp. 5-60.

Tinti S., Tonini R. (2013) The UBO-TSUFD tsunami inundation model: validation and application to a tsunami case study focused on the city of Catania, Italy, Nat. Hazards Earth Syst. Sci., 13, 1795–1816, www.nat-hazards-earth-syst-sci.net/13/1795/2013/, doi: 10.5194/nhess-13-1795-2013.

Tinti, S., Bortolucci, E., and Vannini C.: A block-based theoretical model suited to gravitational sliding, Natural Hazards, 16, 1-28, 1997.

Tinti, S., Pagnoni, G., Zaniboni, F. (2006). The landslides and tsunamis of 30th December 2002 in Stromboli analysed through numerical simulations, Bulletin of Volcanology, 68, 462-479, doi: 10.1007/s00445-005-0022-9.

Tokimatsu, K., Seed, H.B., 1987. Evaluation of settlements in sands due to earthquake shaking. Journal of geotechnical engineering, 113, 861-878.

Tomasello, G., Porcino, D.D., 2022. Influence of sloping ground conditions on cyclic liquefaction behavior of sand under simple shear loading. Soil Dynamics and Earthquake Engineering, 163, 107516.

Tonkin, Taylor, 2012. Canterbury Earthquakes 2010 and 2011: Land Report as at 29 February 2012. . Earthquake, Commission.

Vaid, Y.P., Stedman, J.D., Sivathayalan, S., 2001. Confining stress and static shear effects in cyclic liquefaction. Canadian Geotechnical Journal, 38, 580-591.

Zaniboni F., Armigliato A., Tinti S. (2016). A numerical investigation of the 1783 landslide-induced catastrophic tsunami in Scilla, Italy, Nat. Hazards, 84, 455–470, https://doi.org/10.1007/s11069-016-2461-3.

Zaniboni F., Pagnoni G., Gallotti G., Paparo M.A., Armigliato A., Tinti S. (2019). Assessment of the 1783 Scilla landslide–tsunami's effects on the Calabrian and Sicilian coasts through numerical modelling. Nat. Hazards Earth Syst. Sci., 19, 1585–1600, DOI: https://doi.org/10.5194/nhess-19-1585-2019.

Zaniboni F., Pagnoni G., Paparo M.A., Gauchery T., Rovere M., Argnani A., Armigliato A. and Tinti S. (2021). Tsunamis From Submarine Collapses Along the Eastern Slope of the Gela Basin (Strait of Sicily). Front. Earth Sci. 8:602171. doi: 10.3389/feart.2020.602171.

Zengaffinen-Morris T., Urgeles R., Løvholt F. (2022). On the inference of tsunami uncertainties from landslide run-out observations. Journal of Geophysical Research: Oceans, 127, e2021JC018033. https://doi.org/10.1029/2021JC018033.

Zhang, G., Robertson, P.K., Brachman, R.W., 2002. Estimating liquefaction-induced ground settlements from CPT for level ground. Canadian Geotechnical Journal, 39, 1168-1180.